How Chaos Arises from a Homoclinic Flip Bifurcation

Andrus Giraldo[†], Bernd Krauskopf[†], and Hinke M. Osinga[†]

November 28, 2017

Abstract

Homoclinic bifurcations are organizing centers for the creation of chaotic dynamics. We study a specific homoclinic bifurcation called a homoclinic flip bifurcation of case **C**, where a homoclinic orbit to a saddle equilibrium with real eigenvalues changes from being orientable to nonorientable. This bifurcation is of codimension two, meaning that it can be found as a bifurcation point on a curve of homoclinic bifurcations in a suitable two-parameter plane. In fact, this is the lowest codimension for a homoclinic bifurcation of a real saddle that generates chaotic behavior in the form of (suspended) Smale horseshoes and strange attractors. We present a detailed study of how global stable and unstable manifolds of the saddle equilibrium and of bifurcating periodic orbits interact in the unfolding of the homoclinic flip bifurcation of case **C**. This represents the next and final step in understanding the generic cases of homoclinic flip bifurcations, which started with the study of the simpler cases **A** and **B**. In a three-dimensional vector field due to Sandstede, we compute relevant bifurcation curves in the two-parameter bifurcation diagram near the central codimension-two bifurcation in unprecedented detail. We present representative images of invariant manifolds, computed with a boundary value problem setup, both in phase space and as intersection sets with a suitable sphere. In this way, we are able to identify infinitely many cascades of homoclinic bifurcations that accumulate on specific codimension-one heteroclinic bifurcations between an equilibrium and various saddle periodic orbits. Our computations confirm what is known from theory but also show the existence of different phenomena that were not considered before. Specifically, we identify the boundaries of the Smale–horseshoe region in the parameter plane, one of which creates a strange attractor of Rössler type. The computation of a winding number reveals a complicated overall bifurcation structure that involves infinitely many further homoclinic flip bifurcations associated with so-called homoclinic bubbles.

Keywords— global invariant manifolds, homoclinic tangencies, homoclinic and heteroclinic bifurcations, inclination flip, saddle periodic orbits, chaos

1 Introduction

Homoclinic bifurcations lie at the heart of complicated dynamics in smooth vector fields. Apart from being interesting objects of study in their own right, homoclinic bifurcations appear in many applications, such as mathematical biology [22, 23], laser physics [38, 39]

[†]Department of Mathematics, The University of Auckland, Private Bag 92019, Auckland 1142, New Zealand (a.giraldo@auckland.ac.nz, b.krauskopf@auckland.ac.nz, h.m.osinga@auckland.ac.nz)

and electronic engineering [19]; more on their relevance for applications can be found, for example, in [14]. Indeed, the study of homoclinic bifurcations is important as a first step in the pursuit of understanding complex behavior that arises in mathematical models of different physical phenomena. Since the work of Shilnikov [34] on homoclinic bifurcations to a saddle focus (with complex eigenvalues), which is now called a *Shilnikov bifurcation*, a lot of attention has focused on the consequences of the existence of homoclinic bifurcations. Famously, the Shilnikov bifurcation, subject to certain eigenvalue conditions, is the only homoclinic bifurcation of codimension one that generates chaotic behavior in the form of (suspended) Smale–horseshoe dynamics; see [17] for a comprehensive review. This contrasts the situation of a codimension-one homoclinic bifurcation of a real saddle (with only real eigenvalues), which does not generate any nearby chaotic behavior. However, near the codimension-two homoclinic bifurcation of the real saddle, known as the *homoclinic flip* bifurcation, (suspended) Smale–horseshoes [15] and strange attractors [25, 26] arise when certain eigenvalue and geometric conditions are satisfied. More generally, homoclinic flip bifurcations can be of different cases (discussed below), and these cases act as organizing centers for the creation of periodic orbits and multi-pulse solutions [15]. Specifically, the existence of homoclinic flip bifurcations explains the creation of spiking behavior in mathematical models of neurons such as the Hindmarsh–Rose system [23].

This paper is about the homoclinic flip bifurcation of case **C**, which is the most complicated case that features chaotic dynamics. We consider here the defining situation of a three-dimensional vector field with a real saddle equilibrium. Without loss of generality, we assume that this equilibrium has two different real stable eigenvalues, and one unstable eigenvalue. Generically, at the moment of a codimension-one homoclinic bifurcation of a real saddle equilibrium, the two-dimensional stable manifold forms either a topological cylinder or a Möbius band as it is followed locally around the homoclinic orbit. The homoclinic flip bifurcation is characterized as the moment when this stable manifold changes from orientable to nonorientable [17, 18, 35]. A homoclinic flip bifurcation has different unfoldings depending on the eigenvalues of the saddle equilibrium. In general, three generic cases have been identified, denoted **A**, **B** and **C** [17]. In case **A** a single attracting (or repelling) periodic orbit is created. The unfolding of case **B** involves saddle periodic orbits, a period-doubling bifurcation and an additional homoclinic bifurcation curve nearby [12, 17, 18]. Finally, the unfolding of case **C** gives rise to period-doubling cascades, n-homoclinic orbits, for any $n \in \mathbb{N}$, a region of Smale–horseshoe dynamics [8, 15, 32], and strange attractors [25, 26]. Importantly, case **C** constitutes the homoclinic bifurcation of a real saddle with the lowest codimension that generates chaotic dynamics.

The unfoldings for the three cases have been studied theoretically with different techniques including return maps [8, 15], Shilnikov variables [18] and Lin's method [32]. The unfoldings for both cases **A** and **B** have been determined and proven for any vector field of dimension $n \geq 3$. The exact nature of the unfolding of case **C** is not as well understood as that for cases **A** and **B**; in particular, the complete unfolding is not known because infinitely many saddle periodic orbits are created and the interactions of their respective stable and unstable manifolds give rise to many other global bifurcations. This complexity is associated with the existence of Smale–horseshoes dynamics [8] and is linked to the eigenvalue conditions that defines case **C** [15]. More specifically, cascades of period-doubling and homoclinic bifurcations are featured in the unfolding to explain the annihilation process of the infinitely many saddle periodic orbits that exist in the Smale–horseshoe region [15]. However, the literature does not yet provide an understanding of the boundaries of the Smale–horseshoe region, the nature of additional bifurcations due to interactions of manifolds, or the im-

plications of such interactions for the reorganization of basin of attraction in phase space. Moreover, all results concerning the dynamics and unfolding of case **C** have only been proven for three-dimensional vector fields.

In this paper, we study a homoclinic flip bifurcation of case **C** in unprecedented detail. We use two-point boundary vale problem (2PBVP) continuation techniques [37] for the computation of global invariant manifolds [20] and their interactions. In this way, we are able to present the overall dynamics near a homoclinic flip bifurcation of case **C** in a more global sense. Our focus is on the organization of the three-dimensional phase space by global invariant manifolds of saddle equilibria and saddle periodic orbits. These objects rearrange themselves in sequences of global bifurcations that arise from the codimension-two homoclinic flip bifurcation point of case **C**.

As in previous work for cases **A** [1] and **B** [12], we consider the three-dimensional vector field

$$X^s(x,y,z): \begin{cases} \dot{x} = P^1(x,y,z) := ax + by - ax^2 + (\tilde{\mu} - \alpha z)x(2-3x) + \delta z, \\ \dot{y} = P^2(x,y,z) := bx + ay - \frac{3}{2}bx^2 - \frac{3}{2}axy - 2y(\tilde{\mu} - \alpha z) - \delta z, \\ \dot{z} = P^3(x,y,z) := cz + \mu x + \gamma xz + \alpha\beta(x^2(1-x) - y^2), \end{cases} \tag{1}$$

which was introduced by Sandstede in [33] as a model containing homoclinic flip bifurcations of all three different cases. We choose parameters as discussed in section 2.1, such that the equilibrium located at the origin $\mathbf{0} \in \mathbb{R}^3$ is a saddle with two different real negative (stable) and one positive (unstable) eigenvalues $\lambda^{ss} < \lambda^s < 0 < \lambda^u$. Then the origin has a two-dimensional stable manifold $W^s(\mathbf{0})$ and a one-dimensional unstable manifold $W^u(\mathbf{0})$, which consist of the points in phase space that converge to $\mathbf{0}$ forward and backward in time, respectively. In particular, system eq. (1) is at a homoclinic bifurcation when $W^s(\mathbf{0}) \cap W^u(\mathbf{0}) \neq \emptyset$, that is, at the moment when there exists a trajectory that converges both to $\mathbf{0}$ forward and backward in time. System eq. (1) exhibits a homoclinic bifurcation for $\mu = 0$ [33], which is a homoclinic flip bifurcation of case **C** when $\alpha \approx 0.3694818$. We denote this point by $\mathbf{C_I}$ throughout this paper, and we study the bifurcation diagram of system eq. (1) in the (α, μ)-plane near $\mathbf{C_I}$.

1.1 The codimension-two homoclinic flip orbit

Figure 1 shows phase portraits of system eq. (1) at three different points along the homoclinic bifurcation curve given by $\mu = 0$ in the (α, μ)-plane. The individual panels show the homoclinic orbit together with the associated stable and unstable manifolds of $\mathbf{0}$, where the stable manifold $W^s(\mathbf{0})$ is rendered in two shades of blue to illustrate its orientability; here, every trajectory that forms $W^s(\mathbf{0})$ has arclength four. The homoclinic orbit $\mathbf{\Gamma}_{\text{hom}}$ is the branch of $W^u(\mathbf{0})$ (red curves) that lies in $W^s(\mathbf{0})$. The homoclinic bifurcations in panels (a) and (b) in fig. 1 are of codimension one, because they fullfil the following genericity conditions [15, 18]:

(**G1**) (Non-resonance) $|\lambda^s| \neq \lambda^u$;

(**G2**) (Principal homoclinic orbit) In positive time the homoclinic trajectory approaches the equilibrium tangent to the eigenvector e^s associated with λ^s;

(**G3**) (Strong inclination) The tangent space $\mathrm{T}W^s(\mathbf{0})$ of the stable manifold $W^s(\mathbf{0})$, when followed along $\mathbf{\Gamma}_{\text{hom}}$ backward in time, converges to the plane spanned by the eigenvectors associated with λ^{ss} and λ^u.

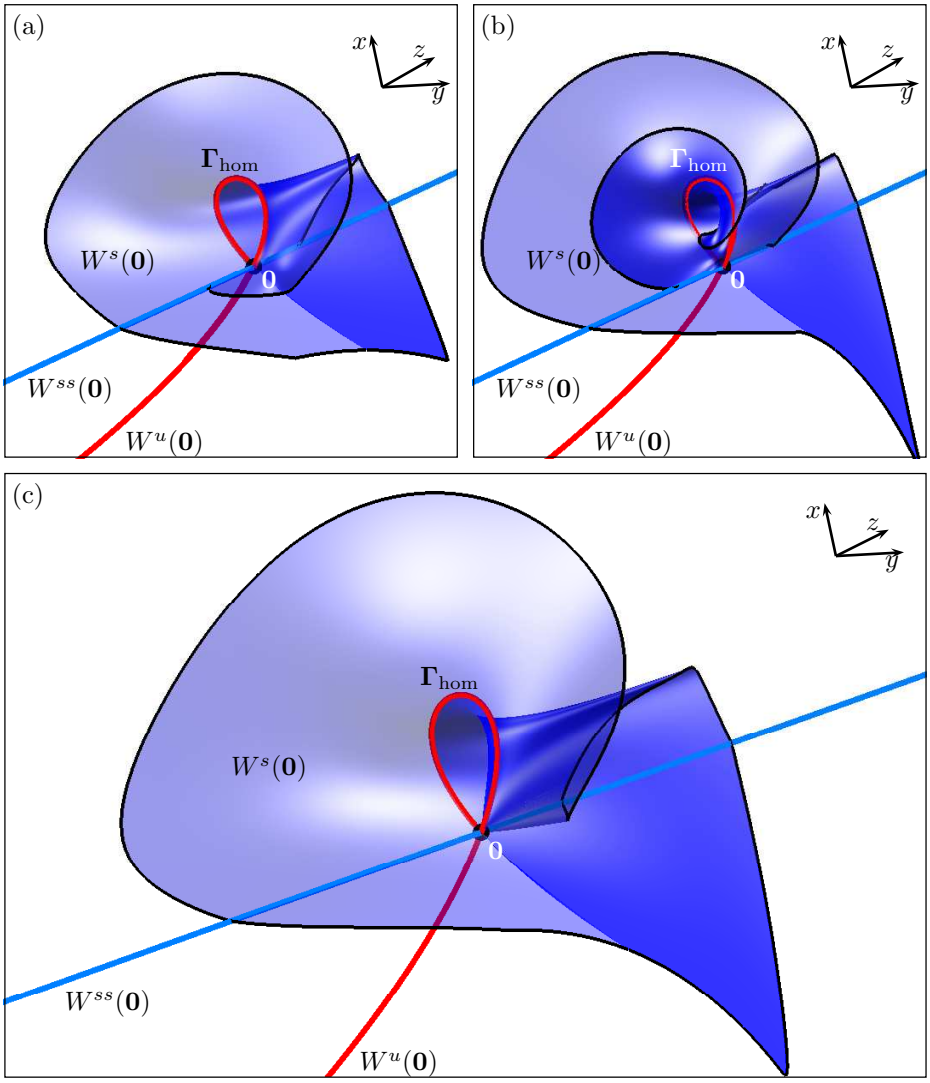

Figure 1: The stable manifold $W^s(\mathbf{0})$ of system eq. (1) in $\mathbb{R}^3$ at a codimension-one orientable and nonorientable homoclinic bifurcation in panels (a) and (b), respectively; panel (c) shows $W^s(\mathbf{0})$ at a codimension-two inclination flip bifurcation. Here, $W^s(\mathbf{0})$ is rendered transparent with one half colored dark blue and the other half light blue. The unstable manifold $W^u(\mathbf{0})$ is colored red and the homoclinic orbit is labeled $\Gamma_{\rm hom}$. The one-dimensional strong stable manifold $W^{ss}(\mathbf{0})$ is highlighted by a blue curve. The common parameter values for all three panels are $(a, b, c, \beta, \gamma, \mu, \tilde{\mu}) = (0.7, 1, -2, 1, 2, 0, 0)$; furthermore, $\alpha = 0.2$ in panel (a), $\alpha = 0.5$ in panel (b) and $\alpha \approx 0.3694818$ in panel (c).

These three properties ensures that a portion of $W^s(\mathbf{0})$ close to $\mathbf{\Gamma}_{\text{hom}}$ folds over and closes along a trajectory of $W^s(\mathbf{0})$ tangent to the strongest stable eigenvector of $\mathbf{0}$, that is, along the strong stable manifold $W^{ss}(\mathbf{0})$ (blue curve); hence, locally near $\mathbf{\Gamma}_{\text{hom}}$, the stable manifold $W^s(\mathbf{0})$ is topologically equivalent to a cylinder, in fig. 1 (a), or a Möbius band, in fig. 1 (b); see [1] for more details. Recall that, for $\mu = 0$, system eq. (1) always exhibits a homoclinic bifurcation; hence, it seems that one can transition between panels (a) and (b) by varying α continuously. However, a cylinder and a Möbius band are not homeomorphic surfaces, so there must exist a transition point, where $W^s(\mathbf{0})$ does not close in either of the two ways depicted in panels (a) and (b). This transition case is shown in panel (c) of fig. 1 for $\alpha \approx 0.3694818$, where a homoclinic flip bifurcation takes place, which is called an *inclination flip* (**IF**). At this bifurcation point genericity condition **(G3)** is not fulfilled and $W^s(\mathbf{0})$ does not close along $W^{ss}(\mathbf{0})$; see fig. 1 (c). It was proven in [8, 15, 18] that the inclination flip bifurcation is one mechanism by which one can transition between the orientable and nonorientable case of a homoclinic bifurcation of codimension one. It is not the only known mechanism: a transition in orientability of the homoclinic bifurcation may also occur via a so called *orbit flip* bifurcation, which corresponds to a homoclinic bifurcation that does not fulfill condition **(G2)**. Both inclination and orbit flip are codimension-two homoclinic flip bifurcations whose unfolding can be of cases **A**, **B** and **C**.

For the purpose of this paper, we only consider the inclination flip bifurcation of case **C**, which occurs if one of the following eigenvalue conditions are satisfied [17]:

$$|\lambda^{ss}| < \lambda^u \quad \text{or} \quad 2|\lambda^s| < \lambda^u, \tag{2}$$

and the following geometric conditions are met:

(i) $|\lambda^s| \neq |\lambda^{ss}|/2$

(ii) If $|\lambda^s| < |\lambda^{ss}|/2$, the homoclinic orbit converges to $\mathbf{0}$ tangent to e^s in a typical way. Geometrically, this means that the homoclinic orbit is not contained in the one-dimensional leading (weak) stable manifold tangent to $\mathbf{0}$, which exists uniquely as a smooth manifold under these eigenvalue conditions; for further details see [17].

(iii) If $|\lambda^s| > |\lambda^{ss}|/2$, the invariant manifold of the homoclinic orbit, which is tangent to the $\text{span}\{e^s, e^u\}$ backward in time, has a nondegenerate quadratic tangency with $W^s(\mathbf{0})$ along the homoclinic orbit.

1.2 Bifurcation diagram of case C

The literature distinguishes between two different unfoldings of a homoclinic flip bifurcation of case **C** [15]. These are given by global conditions regarding the geometry of the stable manifold $W^s(\mathbf{0})$ during the creation of the Smale–horseshoe, and they are called an outward twist $\mathbf{C}_{\text{out}}$ and an inward twist $\mathbf{C}_{\text{in}}$ in the literature [8, 15]. Both twist cases contain the same codimension-one bifurcation curves but their relative positions differ. In particular, we find that the homoclinic flip bifurcation point $\mathbf{C_I}$ found for system eq. (1) corresponds to the outward twist case.

Figure 2 shows a sketch of what is known theoretically about the unfolding of a homoclinic flip bifurcation of case **C** for an outward twist $\mathbf{C_{out}}$ [15, 16]. The unfolding consists of an orientable homoclinic bifurcation curve H_o^1 that becomes nonorientable (twisted) H_t^1 after transitioning through the codimension-two flip bifurcation point $\mathbf{C_{out}}$. Furthermore, the following bifurcation curves emanate from $\mathbf{C_{out}}$: a saddle-node bifurcation SN^1 of periodic

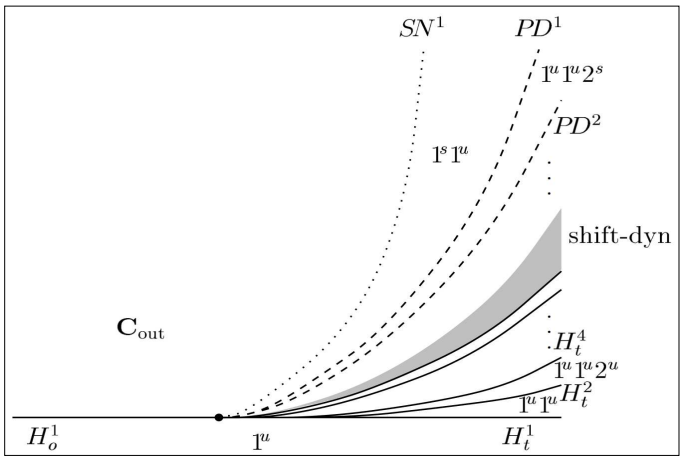

Figure 2: Sketch of the theoretical unfolding of an outward twist point $\mathbf{C_{out}}$ of case **C** from [16, Fig. 5]. [Reproduced from Journal of Dynamics and Differential Equations, Resonant Homoclinic Flip Bifurcations, 12(4), 2000, pages 807-850, A. J. Homburg and B. Krauskopf, ©Plenum Publishing Corporation 2000 with permission of Springer.]

orbits, an infinite sequence of period-doubling bifurcations labeled PD^n, $n = 1, 2, 4, 8, ...$, and an infinite sequence of n-homoclinic bifurcations labeled H_t^n, $n = 2, 4, 8, ...$, where t indicates that these are codimension-one nonorientable (twisted) homoclinic bifurcations. The value of n indicates the number of loops made by the homoclinic orbit before it connects back to the equilibrium point. As each homoclinic bifurcation occurs, a saddle periodic orbit with n loops is created. The Smale–horseshoe region lies in between the period-doubling and homoclinic cascades; however, the boundaries of this region are not identified in the sketch. Note that the orientability of the saddle periodic orbits, labeled 1^u and 2^u, are not explicitly stated in fig. 2, meaning that labels are not unique to each saddle periodic orbit.

To explain the overall structure of the unfolding, we start with the orientable saddle periodic orbit 1^u that bifurcates from the orientable homoclinic bifurcation H_o^1. This same label 1^u is also used for the nonorientable saddle periodic orbit that bifurcates from H_t^1. Note in the sketch that the orientable and nonorientable saddle periodic orbits persist throughout the cascades of period-doubling and homoclinic bifurcations, and they disappear in the saddle-node bifurcation SN^1, after the nonorientable saddle periodic orbit becomes an attracting periodic orbit, labeled 1^s, in the period-doubling bifurcation PD^1. Even though it is not illustrated in fig. 2, the unfolding is known to have infinitely many saddle-node bifurcation curves that also emanate from $\mathbf{C_{out}}$ and occur along the period-doubling cascade [17].

Most of the literature on case **C** does not delve into details about bifurcations related to interactions of manifolds of saddle periodic orbits. This is also the case in fig. 2 where the bifurcation diagram only shows local bifurcations of saddle periodic orbits and homoclinic bifurcations of the real saddle. For ease of exposition and in contrast to fig. 2, we label the orientable saddle periodic orbit that bifurcates from H_o^1 as Γ_o, and the nonorientable saddle periodic orbit that bifurcates from H_t^1 as Γ_t throughout this paper.

1.3 Computing the bifurcation diagram near $\mathbf{C_I}$

By computing the interaction of the manifolds of these saddle periodic orbits with other objects, we are able to present the unfolding of case **C** in a new light. Throughout this paper, we center our attention on the saddle periodic orbits Γ_o and Γ_t, and their corre-

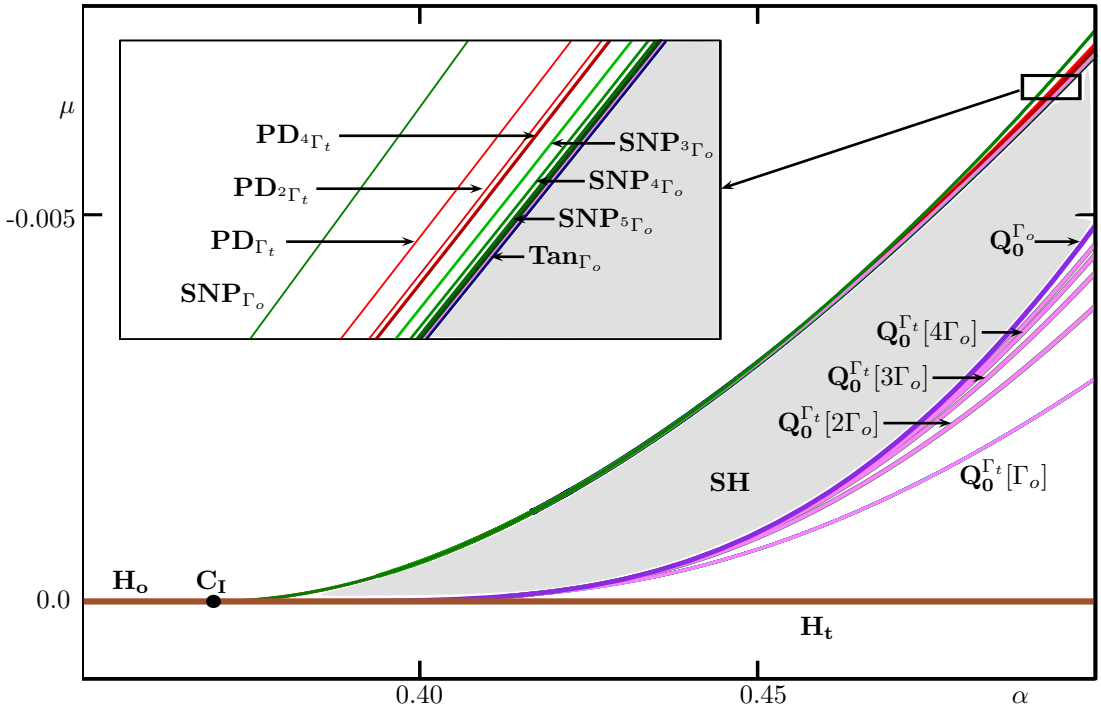

Figure 3: Bifurcation diagram in the (α, μ)-plane near an homoclinic flip bifurcation $\mathbf{C_I}$ of system eq. (1). The inset shows an enlargement of the indicated area. Shown are the curves of homoclinic bifurcation $\mathbf{H_o}$ and $\mathbf{H_t}$ (brown), saddle-node bifurcations **SNP** of periodic orbits (dark-green), period-doubling bifurcations **PD** (red), heteroclinic bifurcations $\mathbf{Q_0^{\Gamma_t}}$ from $\mathbf{0}$ to Γ_t (magenta), heteroclinic bifurcation $\mathbf{Q_0^{\Gamma_o}}$ from $\mathbf{0}$ to Γ_o (purple) and codimension-one homoclinic bifurcation bifurcation $\mathbf{Tan}_{\Gamma_o}$ of Γ_o (violet). The Smale–horseshoe region **SH** is the gray region. The other parameter values are $(a, b, c, \beta, \gamma, \tilde{\mu}, \delta) = (0.7, 1, -2, 1, 2, 0, 0)$.

sponding global manifolds. As a starting point, we show in fig. 3 the bifurcation diagram for system eq. (1) in the (α, μ)-plane near the homoclinic flip point $\mathbf{C_I}$ of case **C**. Note that we changed the orientation of the μ-axis from top to bottom in the bifurcation diagram for ease of comparison. Figure 3 shows the principal homoclinic branch (brown curve) together with representative period-doubling **PD** (red curves) and saddle-node **SNP** (green curves) bifurcations of periodic orbits. To exemplify the relevance of the global bifurcations concerning saddle periodic orbits, we also compute representative codimension-one heteroclinic and homoclinic bifurcations in system eq. (1) of the saddle periodic orbits Γ_o and Γ_t, labelled $\mathbf{C_0^{\Gamma_o}}$ and $\mathbf{Q_0^{\Gamma_t}}[m\Gamma_o]$ for $m = 1, 2, 3, 4$. At first glance, the period-doubling and saddle-node bifurcation curves are indiscernible near the inclination flip point $\mathbf{C_I}$ in fig. 3. To visualize these curves, the inset shows an enlargement of a region of the bifurcation diagram that distinguishes the first three computed period-doubling bifurcation $\mathbf{PD}_{\Gamma_t}$, $\mathbf{PD}_{2\Gamma_t}$ and $\mathbf{PD}_{4\Gamma_t}$ of a period-doubling cascade. Furthermore, it shows the saddle-node bifurcation curves $\mathbf{SNP}_{\Gamma_o}$, $\mathbf{SNP}_{3\Gamma_o}$, $\mathbf{SNP}_{4\Gamma_o}$ and $\mathbf{SNP}_{5\Gamma_o}$ which are responsible for the disappearance of the orientable saddle periodic orbits created during the homoclinic cascade, as will be discussed in detail in section 5. For the remainder of this paper, the subindices in the label of each saddle-node bifurcation **SNP** of periodic orbits refers to the orientable saddle period orbit involved. The same applies to the period-doubling bifurcations **PD**, where the subindices refer to the corresponding nonorientable saddle periodic orbit involved. Note how the saddle-node bifurcation curves accumulate onto the codimension-one homoclinic bifurcation $\mathbf{Tan}_{\Gamma_o}$ (violet curve) of Γ_o where the stable and unstable manifolds of Γ_o have a quadratic tangency. We identify the curve $\mathbf{Tan}_{\Gamma_o}$ as one of the boundaries of the Smale–horseshoe region **SH** (gray region), as it delimits the region in the bifurcation diagram where there exist structurally stable homoclinic orbits of Γ_o.

Overall, the computed fig. 3 agrees well with the sketch in fig. 2; however, one of the most apparent differences are the curves $\mathbf{Q_0^{\Gamma_t}}[m\Gamma_o]$, with $m = 1, 2, 3, 4$, of heteroclinic connecting orbits between $\mathbf{0}$ and Γ_t (magenta curves). For each of these heteroclinic bifurcation curves, we find infinitely many homoclinic and heteroclinic bifurcation curves accumulating on it; these are not shown in fig. 3 because they lie very close to the curves $\mathbf{Q_0^{\Gamma_t}}[m\Gamma_o]$. We describe in more detail these accumulation cascades in section 5. Notice in fig. 3 how the sequence of heteroclinic bifurcation curves $\mathbf{Q_0^{\Gamma_t}}[m\Gamma_o]$ accumulates onto the heteroclinic bifurcation $\mathbf{Q_0^{\Gamma_o}}$ (purple curve) of a heteroclinic connecting orbit between $\mathbf{0}$ and Γ_o, which corresponds to the other boundary of the Smale–horseshoe region **SH** in the bifurcation diagram. Both boundary curves, $\mathbf{Tan}_{\Gamma_o}$ and $\mathbf{Q_0^{\Gamma_o}}$, were not included or studied in the theoretical unfolding as shown in fig. 2. Furthermore, the bifurcation $\mathbf{Tan}_{\Gamma_o}$ acts as mechanism to destroy a strange attractor, which was conjectured to exist close to the inclination flip point due to the cascades of period-doubling and saddle-node bifurcation [25, 26]; this will be discussed in more detail in section 7.

The main purpose of this paper is to obtain an overall understanding of the unfolding of the inclination flip bifurcation point $\mathbf{C_I}$ of case **C** through a detailed study of the role of representative invariant manifolds in the reorganization of phase space as different codimension-one bifurcations occur. Of particular interest is to understand the nature and roles of the infinitely many cascades of codimension-one homoclinic and heteroclinic bifurcations, the boundaries in parameter plane of the Smale–horseshoe regions, and the existence and annihilation of strange attractors, etc. To present our results, we choose parameter values in (α, μ)-plane close to $\mathbf{C_I}$ and provide representative figures of the relevant objects in phase space, as well as their intersection sets with a suitable sphere. This allows us to show the consequences of different codimension-one bifurcations for the organization of

phase space, and to present an overall picture of the unfolding of $\mathbf{C_I}$ in the (α, μ)-plane. Motivated by the existence of infinitely many homoclinic and heteroclinic bifurcation, we define a winding number ζ as a topological invariant for system eq. (1). A two-parameter sweep in the (α, μ)-plane identifies open regions with constant ζ-values close to $\mathbf{C_I}$. Their respective boundaries correspond to codimension-one homoclinic bifurcation curves. Hence, this parameter sweep contributes to obtaining a clearer picture of how the infinitely many homoclinic bifurcation are organized and accumulate onto heteroclinic bifurcations curves of the saddle periodic orbit Γ_t. Furthermore, we identify and characterize a phenomenon where two different homoclinic bifurcation curves emanating from $\mathbf{C_I}$ meet and create a "homoclinic bubble" [16] in the (α, μ)-plane as we consider a larger parameter range in the (α, μ)-plane.

The organization of this paper is as follows. In section 2 we introduce some notation; here, we also present the parameter values used, and give the definition of the winding number ζ. We present, in section 3, the bifurcation diagram of system eq. (1) near $\mathbf{C_I}$. Section 4 then focusses on the transition through the main codimension-one homoclinic bifurcation curve, section 5 on the homoclinic and heteroclinic cascades, section 6 on the Smale–horseshoe region, and section 7 on the period-doubling cascade and the existence of an strange attractor of Rössler type. Finally, we characterize, in section 8, the bubble phenomenon arising in the bifurcation diagram of $\mathbf{C_I}$. We end in section 9 with a discussion and an outlook on future research.

The computations in this paper are performed with the pseudo-arclength continuation package AUTO [9, 10] and its extension HOMCONT [7]. More specifically, global manifolds are computed with a two-point boundary value problem set-up [5, 20] and the heteroclinic orbits are obtained with Lin's method [21, 42]. The parameter sweeping of ζ in parameter plane, visualization and post-processing of the data are performed with MATLAB®.

2 Notation and set-up

We choose parameters such that the Jacobian $Df(\mathbf{0})$ of $\mathbf{0}$ has two stable and one unstable eigenvalues, $\lambda^{ss} < \lambda^s < 0 < \lambda^u$ with eigenvectors e^{ss}, e^s and e^u, respectively. The global stable manifold $W^s(\mathbf{0})$ is a surface foliated by trajectories that converge to $\mathbf{0}$ as $t \to \infty$, and global unstable manifold $W^u(\mathbf{0})$ consist of two trajectories that converge to $\mathbf{0}$ as $t \to -\infty$. The manifold $W^s(\mathbf{0})$ and $W^u(\mathbf{0})$ are immersed manifolds in $\mathbb{R}^3$: they are as smooth as f and tangent to the linear spaces spanned by the stable and unstable eigenvectors of $\mathbf{0}$, respectively [30]. Furthermore, associated with λ^{ss}, there is a unique one-dimensional strong stable manifold $W^{ss}(\mathbf{0}) \subset W^s(\mathbf{0})$, defined as the subset of points on $W^s(\mathbf{0})$ that converges to $\mathbf{0}$ tangent to the eigenvector e^{ss}.

System eq. (1) has a second equilibrium $\mathbf{q}$ for the parameters chosen, which is a stable focus that lies near $\mathbf{0}$. We denote its basin of attraction as $\mathcal{B}(\mathbf{q})$. The set $\mathcal{B}(\mathbf{q})$ is an open connected set of $\mathbb{R}^3$ and consists of all points in phase space that converge to $\mathbf{q}$. We also denote by $W^{ss}(\mathbf{q}) \subset \mathcal{B}(\mathbf{q})$ the subset of points that converge to $\mathbf{q}$ tangent to the eigenvector associated with the real eigenvalue of $\mathbf{q}$, which is the largest eigenvalue in modulus.

Let Γ be a periodic orbit of system eq. (1). We denote the two nontrivial Floquet multipliers of Γ by $\Lambda_1, \Lambda_2 \in \mathbb{C}$; they are the eigenvalues of the variational equation of system eq. (1) along Γ at time T, where T is the period of Γ. Note that the Floquet multipliers of Γ in a three-dimensional vector field are always such that their real parts have the same sign; each one has an associated eigenfunction that is referred as the Floquet bundle [36]. If $\Lambda_1, \Lambda_2 \in \mathbb{R}$ and $0 < |\Lambda_1| < 1 < |\Lambda_2|$ then one speaks of a saddle periodic

a	b	c	β	γ	$\tilde{\mu}$	δ
0.7	1.0	-2.0	1.0	2.0	0.0	0.0

Table 1: Parameter values chosen for an inclination flip of case **C** in system eq. (1).

orbit. A saddle periodic orbit has stable $W^s(\Gamma)$ and unstable $W^u(\Gamma)$ manifolds which consist of points that converge to Γ backward and forward in time, respectively. As for the saddle equilibrium case, the associated stable and unstable manifolds of a saddle periodic orbit are two dimensional immersed manifolds; they are tangent to the Floquet bundle of the periodic orbit associated with Λ_1 and Λ_2, respectively [30]. If $0 < \Lambda_1 < 1 < \Lambda_2$, one speaks of an orientable saddle periodic orbit, which we denote by Γ_o, and its stable and unstable manifolds $W^s(\Gamma_o)$ and $W^u(\Gamma_o)$, respectively, are topological cylinders [28, 36]. Similarly, if $\Lambda_2 < -1 < \Lambda_1 < 0$, then the saddle periodic orbit is nonorientable, denoted Γ_t, and $W^s(\Gamma_t)$ and $W^u(\Gamma_t)$ are locally topological Möbius bands [28, 36].

Let S_1, S_2, S_3 be hyperbolic saddle invariant objects of system eq. (1) with manifolds $W^u(S_1)$, $W^s(S_2)$, $W^u(S_2)$ and $W^s(S_3)$ that are all two-dimensional. If there exist structurally stable heteroclinic orbits from S_1 to S_2 and from S_2 to S_3, that is, if $W^u(S_1) \cap W^s(S_2)$ and $W^u(S_2) \cap W^s(S_3)$ are non-empty transversal intersections, then we use the notation $S_1 \to S_2 \to S_3$ to represent this situation.

2.1 Sandstede's Model

System eq. (1) was constructed specifically to study different homoclinic flip bifurcations in three-dimensional vector fields [33]. It is a very convenient vector field, because its parameter can be chosen in such a way that either one of the cases **A**, **B** and **C** occur for both inclination and orbit flip bifurcations. System eq. (1) has been used extensively, particularly to study numerically transitions between the three cases as codimension-three phenomena due to resonance [27], and to investigate the unfoldings of homoclinic flip bifurcations of cases **A** and **B** [1, 12].

Note that $\mathbf{0}$ is an equilibrium of X^s for all parameter values. We use the parameter ranges found in [27] as a reference to study case **C** in the (α, μ)-plane and fix parameters as given in table 1. Since $\delta = 0$, the z-axis is invariant under the flow of system eq. (1) and the eigenvalues of $\mathbf{0}$ are given by

$$\lambda_{1,2} = a \pm \sqrt{b^2 + 4\tilde{\mu}^2} \text{ and } \lambda_3 = c.$$

The inclination flip bifurcation point $\mathbf{C_I}$ of case **C** unfolds with respect to α and μ. At $\mathbf{C_I}$, the equilibrium $\mathbf{0}$ has eigenvalues $\lambda_1 = 1.7$, $\lambda_2 = -0.3$ and $\lambda_3 = -2$, which confirms that $2|\lambda^s| < \lambda^u$ as required for case **C**. Note that the strong stable manifold $W^{ss}(\mathbf{0})$ is the z-axis.

For our chosen parameters, there exists a stable equilibrium $\mathbf{q}$, which is the same equilibrium that appears in the discussion of cases **A** and **B** in [1, 12]. However, unlike for these two cases, the stability of $\mathbf{q}$ is not of relevance in our study of case **C**. More specifically, we find that the orientable saddle periodic orbit Γ_o takes on the role of $\mathbf{q}$; in particular it is responsible for the creation of a fold bifurcation **F** in case **C**. For the case **C** considered in this paper, the equilibrium $\mathbf{q}$ is attracting and identifying its basin of attraction is critical for understanding the reorganization of phase space close to $\mathbf{C_I}$; see section 3.

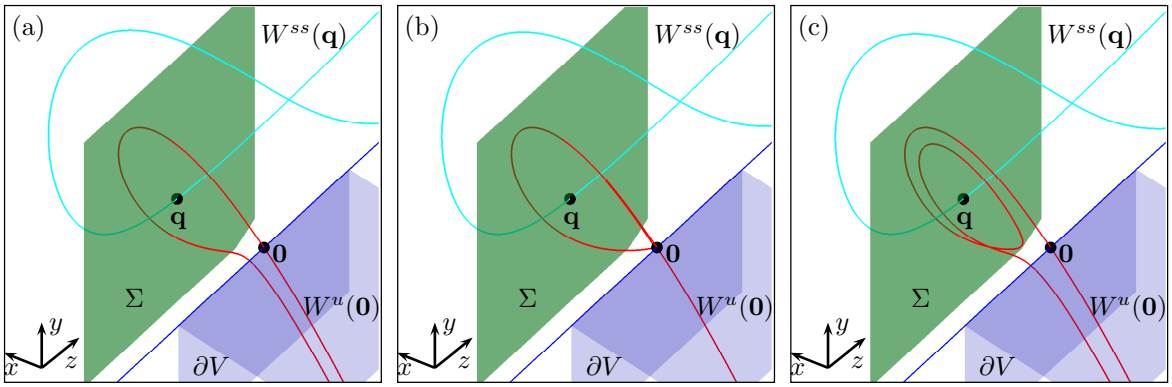

Figure 4: Illustration of the change of the winding number ζ for system eq. (1). Shown are $W^u(\mathbf{0})$ (red curve), $W^{ss}(\mathbf{0})$ (dark-blue curve) and $W^{ss}(\mathbf{q})$ (cyan curve), Σ (green plane), the boundaries ∂V (blue planes). The parameter values are $\mu = 0.001$, $\mu = 0.0$ and $\mu = -0.001$ for panels (a), (b) and (c), respectively. Furthermore, $\alpha = 0.5$ and the other parameter values are as given in table 1.

2.2 Definition of the winding number

The unfolding of an inclination flip bifurcation of case **C** is characterized by the existence of k-homoclinic orbits for any $k \in \mathbb{N}$ [15]. In [27], these codimension-one homoclinic bifurcations in the parameter plane are studied via the continuation of solutions to a suitable two-point boundary value problem (2PBVP) during the transition between cases **B** and **C**. A drawback of this technique is the limitation of sampling only a small number of these bifurcation curves, which increases the risk of missing subtle interactions in the parameter plane. We define a winding number ζ for system eq. (1) and run a two-parameter sweep in the (α, μ)-plane to complement the 2PBVP approach of finding bifurcation curves. The value for ζ is defined as the number of rotations that $W^u(\mathbf{0})$ makes around $W^{ss}(\mathbf{q})$, as introduced more formally below. Parameter sweeping techniques have been used in part to understand the nature of cascades of homoclinic bifurcation close to Bykov T-points in the Lorenz system [4] and Shimizu-Morioka system [4, 41]. It is also useful to illustrate spike adding in neuron models; for example, see [2, 3]. By combining continuation and parameter sweeping, we are able to characterize different phenomena not only in the vicinity of the homoclinic flip bifurcation point of case **C**, but also far away from it.

To define the quantity ζ, let $V := \{p = (x, y, z) \in \mathbb{R}^3 \mid x \leq 0 \text{ and } y \leq 0\}$ and let ∂V be its boundary. Since we set $b = 1 > 0$ and $\delta = 0$ in table 1, we have $\dot{x} < 0$ on $\{x = 0\} \cap V \setminus \{y = 0\}$ and $\dot{y} < 0$ on $\{y = 0\} \cap V \setminus \{x = 0\}$. Furthermore, the z-axis, $\{x = 0\} \cap \{y = 0\}$, is a subset of V and it is invariant. Hence, V is a positively invariant set for system eq. (1), i.e., $\phi^t(V) \subset V$ for all $t \geq 0$ where ϕ^t is the flow defined by system eq. (1). Therefore, any intersection of $W^u(\mathbf{0})$ with ∂V must be transversal and $W^{ss}(\mathbf{q})$ cannot intersect ∂V. We view ζ, that is, the number of rotations that $W^u(\mathbf{0})$ makes around $W^{ss}(\mathbf{q})$, as a kind of linking number, which can only vary through bifurcation. Indeed, since $W^{ss}(\mathbf{q})$ never intersects ∂V and $W^u(\mathbf{0})$ cannot follow $W^{ss}(\mathbf{q})$ to undo itself by restriction of the flow of system eq. (1), we may view these orbits segments as topological closed curves by identifying their endpoints.

Homoclinic bifurcations are a mechanism for ζ to change, as is illustrated in fig. 4 for system eq. (1) with $\alpha = 0.5$ and three different values of μ. In panel (a) the manifold $W^u(\mathbf{0})$ loops once around $W^{ss}(\mathbf{q})$ before reaching ∂V, that is, $\zeta = 1$. As μ decreases, system eq. (1)

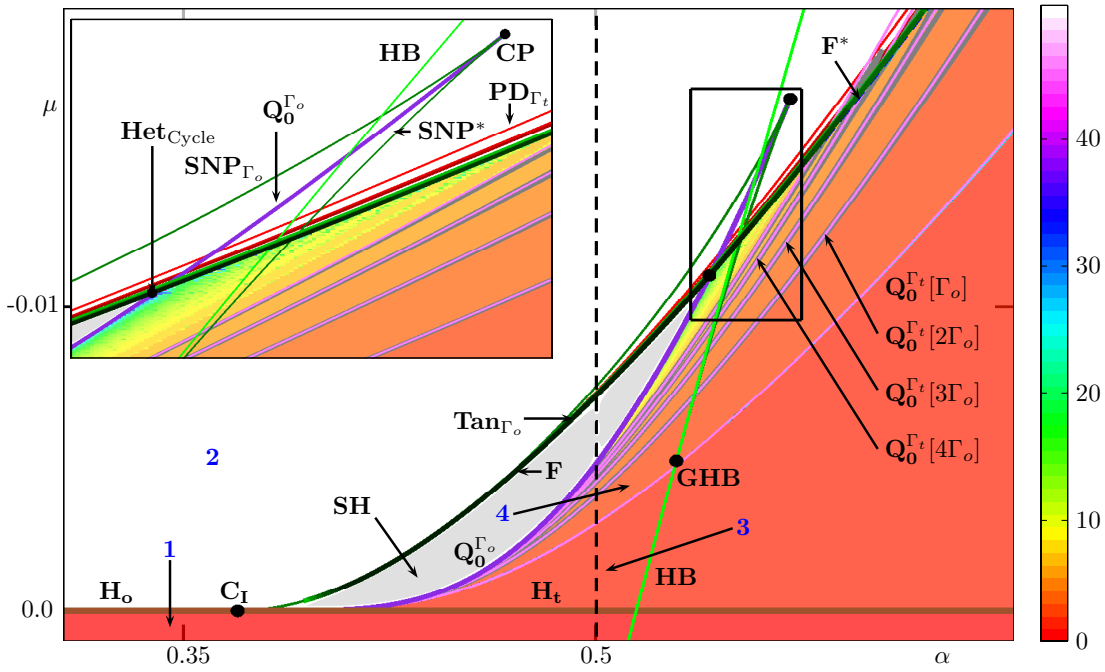

Figure 5: Bifurcation diagram in the (α, μ)-plane near an inclination flip bifurcation $\mathbf{C_I}$ of case **C** of system eq. (1), with coloring of regions according to the winding number ζ as given by the colorbar. The inset shows an enlargement of the region indicated in the main panel. Shown are the curves of homoclinic bifurcation $\mathbf{H_o}$ and $\mathbf{H_t}$ (brown), non-principal homoclinic bifurcation (cyan), saddle-node bifurcation $\mathbf{SNP}_{\Gamma_o}$ and $\mathbf{SNP}^*$ of periodic orbits (dark green), Hopf bifurcation **HB** (light green), period-doubling bifurcation **PD** (red), fold bifurcation curve **F** of heteroclinic orbits from Γ_o to **0** (blue) and its extension $\mathbf{F}^*$ (blue dashed curve), heteroclinic bifurcation $\mathbf{Q_0^{\Gamma_t}}$ from **0** to Γ_t (magenta), heteroclinic bifurcation $\mathbf{Q_0^{\Gamma_o}}$ from **0** to Γ_o (purple) and codimension-one homoclinic bifurcation $\mathbf{Tan}_{\Gamma_o}$ of Γ_o (violet). The curves $\mathbf{SNP}_{\Gamma_o}$ and $\mathbf{SNP}^*$ meet at the cusp point **CP**, and $\mathbf{SNP}^*$ ends at the generalized Hopf bifurcation point **GHB**. The curve **F** meets $\mathbf{Q_0^{\Gamma_o}}$ at a codimension-two heteroclinic cycle point $\mathbf{Het}_{\text{Cycle}}$; the Smale–horseshoe region **SH** (gray region) is indicated. We denote by **1**, **2**, **3** and **4** four different regions close to the $\mathbf{C_I}$ point and the line $\alpha = 0.5$ (dashed). The other parameters are as in table 1.

goes through a homoclinic bifurcation at $\mu = 0$ in panel (b), after which $W^u(\mathbf{0})$ makes an extra turn around $W^{ss}(\mathbf{0})$ before intersecting ∂V, as shown in panel (c); hence, ζ increases to 2.

In practice, we calculate ζ by counting the number of intersections of $W^u(\mathbf{0})$ with $\Sigma := \{(x, y, z) \in \mathbb{R}^3 : x = \mathbf{q}_x\}$, where $\mathbf{q}_x$ is the x-component of $\mathbf{q}$, and dividing this number by two; see fig. 4. The parameter sweeps of ζ shown in figs. 5, 21 and 22 are performed on a 1000×1000 grid over the corresponding parameter ranges.

3 Bifurcation diagram near $\mathbf{C_I}$

We now present more details of the bifurcation diagram shown in fig. 3. Namely, fig. 5 shows it over a slightly larger range of the (α, μ)-plane together with the parameter sweep of ζ where the colors indicate the value of the winding number ζ; the inset shows an enlargement of the indicated region of the main panel. At first glance, we distinguish the curves of

period-doubling, saddle-node and heteroclinic bifurcations presented in fig. 3. Recall that the subindices in the label of each saddle-node bifurcation **SNP** and period-doubling bifurcation **PD** of periodic orbits refers to the orientable and nonorientable saddle period orbit involved, respectively. Specifically for this bifurcation diagram, we only compute and label one of the infinitely many saddle-node and period-doubling curves that emanate from $\mathbf{C_I}$, namely, the saddle-node bifurcation $\mathbf{SNP}_{\Gamma_o}$ of Γ_o (green curve) and period-doubling bifurcation $\mathbf{PD}_{\Gamma_t}$ of Γ_t (red curve).

We now discuss the overall features of the bifurcation diagram in fig. 5; further details will be presented in later sections. Note that, in between successive curves $\mathbf{Q_0^{\Gamma_t}}[m\Gamma_o]$, with $m = 1, 2, 3, 4$, of heteroclinic connecting orbits between $\mathbf{0}$ and Γ_t (magenta curves), there exist big regions of the (α, μ)-parameter plane with constant values of ζ. The value of ζ in these regions increases as we approach the bifurcation $\mathbf{Q_0^{\Gamma_o}}$ (purple) of a heteroclinic connecting orbit between $\mathbf{0}$ and Γ_o. This indicates the existence of more bifurcation curves $\mathbf{Q_0^{\Gamma_t}}[m\Gamma_o]$, for $m > 4$. The labels of the codimension-one heteroclinic bifurcation are deliberately chosen to encode information of the corresponding heteroclinic orbit in phase space. Figure 6 shows, in phase space, representative heteroclinic orbits $\mathbf{Q_0^{\Gamma_t}}$ and $\mathbf{Q_0^{\Gamma_o}}$ (red curves) together with the saddle periodic orbits Γ_t (purple curve) and Γ_o (green curve) at the moment of the corresponding heteroclinic bifurcation. For simplicity, we use the same label of the heteroclinic bifurcation to refer to the corresponding orbit in phase space. The heteroclinic orbit is formed by one branch of $W^u(\mathbf{0})$, which is the branch shown in fig. 6. In panel (a1), the heteroclinic orbit $\mathbf{Q_0^{\Gamma_t}}[\Gamma_o]$ makes an excursion close to the (x, y)-plane, and then follows Γ_o for one rotation before accumulating onto Γ_t. In panels (a2)-(a5), the branch of $W^u(\mathbf{0})$ also accumulates onto Γ_t, but only after making two, three, four and five rotations near Γ_o, respectively. Hence, the number of rotations that the respective heteroclinic orbit of $\mathbf{Q_0^{\Gamma_t}}$ makes in phase space around Γ_o increases until it reaches its limiting case, where the number of rotations around Γ_o has increased to infinity, at $\mathbf{Q_0^{\Gamma_o}}$ as shown in panel (b). This accumulation is seen in fig. 5, where the cascade $\mathbf{Q_0^{\Gamma_t}}[m\Gamma_o]$ accumulate on the final codimension-one heteroclinic bifurcation $\mathbf{Q_0^{\Gamma_o}}$ of a connecting orbit between $\mathbf{0}$ and Γ_o (dark-purple curve). Note also that the winding number ζ is at its computational maximum after this curve; this is due to the accumulation of the unstable manifold $W^u(\mathbf{0})$ onto $\mathbf{q}$ after $\mathbf{Q_0^{\Gamma_o}}$ is crossed, as will be detailed in section 6. This curve $\mathbf{Q_0^{\Gamma_o}}$ represents the last moment where system eq. (1) exhibits a homoclinic or heteroclinic bifurcation close to $\mathbf{C_I}$, after which the dynamics are complicated due to the existence of structurally stable homoclinic orbits of Γ_o.

It was proved under the conditions of case **C** that a Hénon-like attractor unfolds from $\mathbf{C_I}$ [25]. The Smale–horseshoe region was conjectured to be bounded by a first quadratic tangency between the stable and unstable manifolds of a saddle periodic orbit. However, it was not even clear at the time that such a first tangency existed in the unfolding of an inclination flip point. We have found this first tangency and it corresponds to the bifurcation curve $\mathbf{Tan}_{\Gamma_o}$ (violet curve) in fig. 5 where the stable and unstable manifolds of Γ_o have a quadratic tangency. After leaving the Smale–horseshoe region through $\mathbf{Tan}_{\Gamma_o}$, we find a strange attractor in phase space that is topologically equivalent to the Rössler attractor. This attractor exists during a reverse period-doubling cascade which terminates at the bifurcation $\mathbf{PD}_{\Gamma_t}$, where the saddle periodic orbit Γ_t changes to an attracting periodic orbit Γ_t^a and the corresponding attracting periodic orbit ${}^2\Gamma_t^a$ of twice the period disappears. Then Γ_t^a disappears in the saddle-node bifurcation $\mathbf{SNP}_{\Gamma_o}$ with Γ_o.

Note in fig. 5 that we also find a bifurcation curve **F**, similar to the ones found in [1, 12], that represents the moment when $W^s(\mathbf{0})$ becomes tangent to $W^u(\Gamma_o)$. If one follows the

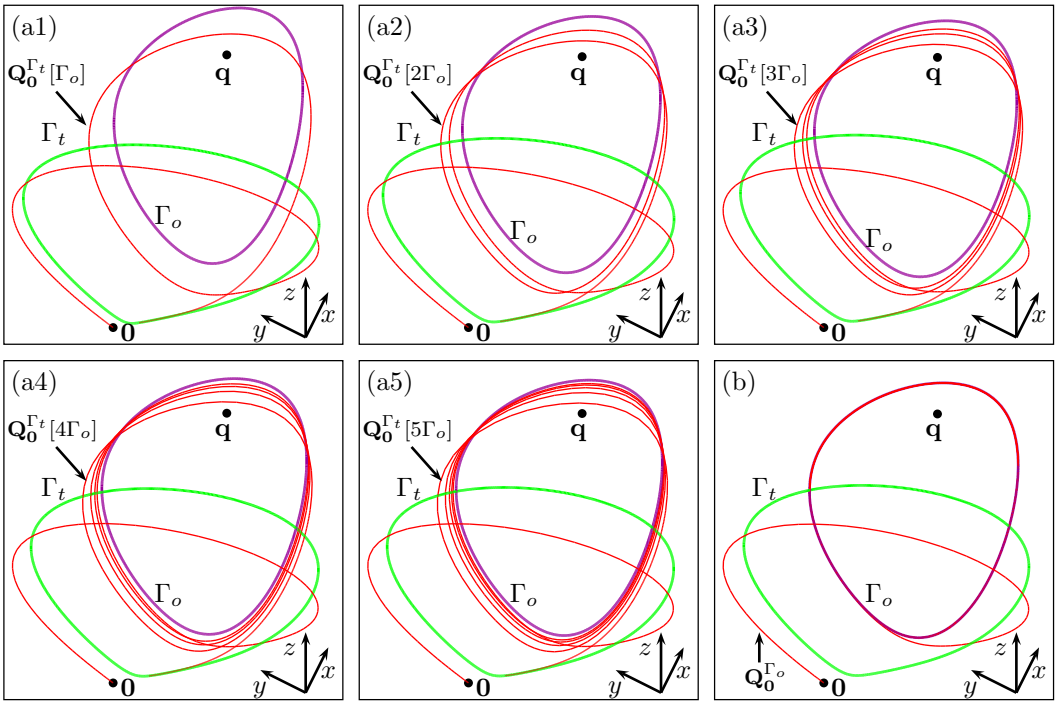

Figure 6: Configuration of the unstable manifold $W^u(\mathbf{0})$ of system eq. (1) in $\mathbb{R}^3$ at the codimension-one heteroclinic bifurcations. Shown are the heteroclinic branch of $W^u(\mathbf{0})$ (red), and the periodic orbits Γ_o (purple) and Γ_t (green). Panels (a1)-(a5) illustrate connections from $\mathbf{0}$ to Γ_t and panel (b) shows the connection from $\mathbf{0}$ to Γ_o. Here, we used $\alpha = 0.5$ and the respective μ-values for each panel are given in table 3.

curve **F** in fig. 5, one sees that it intersects the curve $\mathbf{Q}_{\mathbf{0}}^{\Gamma_o}$ at a point that we labeled $\mathbf{Het}_{\text{Cycle}}$ which is seen more clearly in the corresponding enlargement. At this point, there exists a codimension-two heteroclinic cycle between $\mathbf{0}$ and Γ_o in system eq. (1). The unfolding of this cycle has been studied theoretically [6, 24] as an organizing center for the creation of chaotic regions in the parameter plane and the creation of multi-pulse homoclinic solutions that exhibit flip bifurcations close to it. This agrees with our computations because the Smale–horseshoe region **SH** in fig. 5 also unfolds from the point $\mathbf{Het}_{\text{Cycle}}$; moreover, different homoclinic bifurcation branches in the bifurcation diagram exhibit inclination flip bifurcations as will be discussed in detail in section 8.

Finally, note in fig. 5 that the additional stable equilibrium $\mathbf{q}$ of system eq. (1) goes through a Hopf bifurcation labeled **HB** (light-green curve) and becomes an unstable saddle focus. On the curve **HB**, there exists a generalized Hopf bifurcation point **GHB**, which gives rise to a curve (dark-green) of saddle-node bifurcation $\mathbf{SNP}^*$ at which Γ_o and an attracting periodic orbit Γ^a are created. The curve $\mathbf{SNP}^*$ ends in a cusp bifurcation point **CP** with the curve $\mathbf{SNP}_{\Gamma_o}$; see the inset in fig. 5. The periodic orbits Γ_o and Γ_t disappear on the other side of $\mathbf{SNP}_{\Gamma_o}$ and only Γ^a persists; hence, the bifurcation curves $\mathbf{Q}_{\mathbf{0}}^{\Gamma_o}$ and **F** disappear at the point **CP** and the curve $\mathbf{SNP}^*$, respectively. In particular, we find another curve $\mathbf{F}^*$ (dashed blue line), which represents the moment when $W^s(\mathbf{0})$ becomes tangent to $W^u(\mathbf{q})$; this curve constitutes the extension of **F** past its intersection with $\mathbf{SNP}^*$.

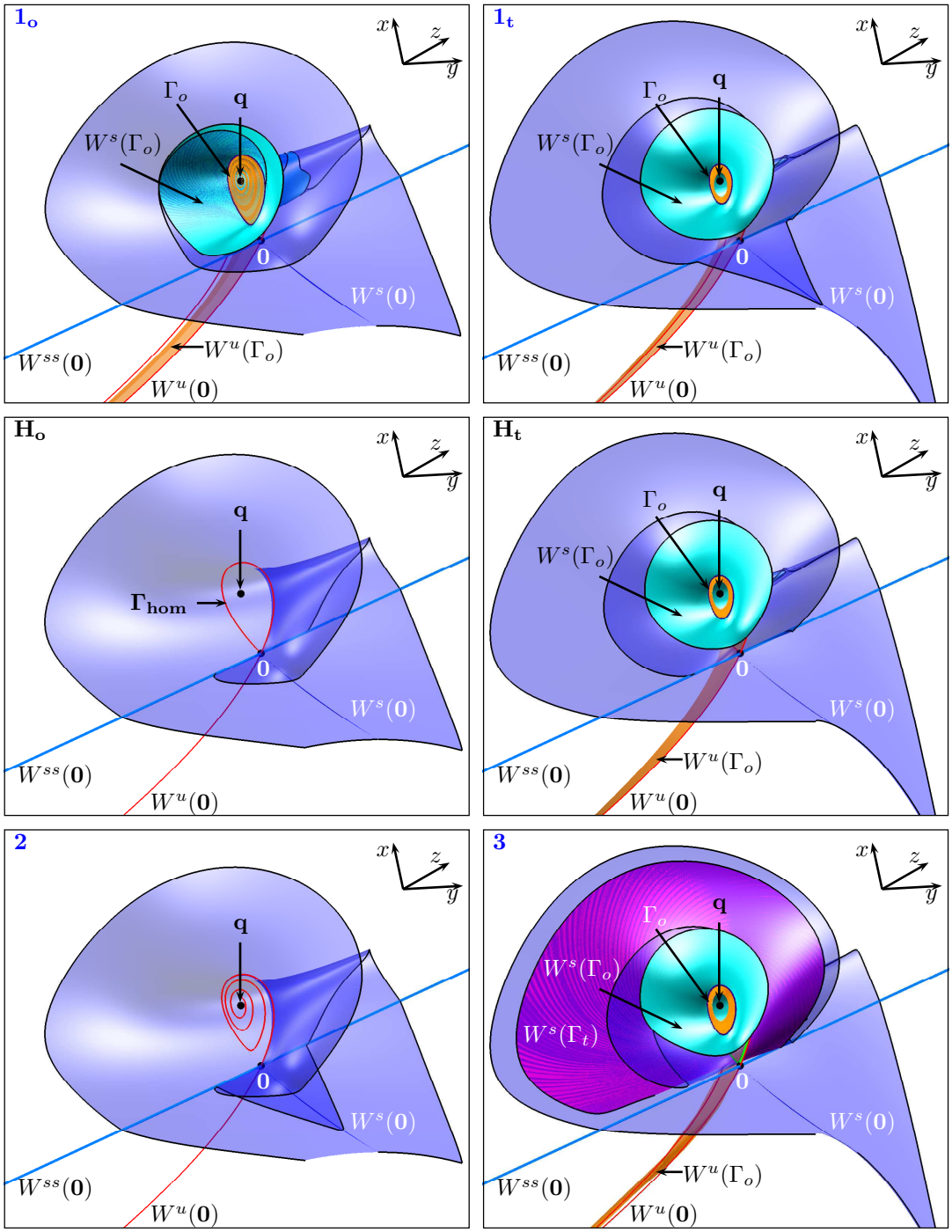

Figure 7: Phase portraits of system eq. (1) in regions **1**–**3** of the (α, μ)-plane and along the bifurcations $\mathbf{H_o}$ and $\mathbf{H_t}$ near the inclination flip point $\mathbf{C_I}$. Shown are $W^s(\mathbf{0})$ (blue surface), $W^{ss}(\mathbf{0})$ (blue curve), $W^u(\mathbf{0})$ (pink curve), $W^s(\Gamma_o)$ (cyan surface) and $W^s(\Gamma_t)$ (purple surface). The (α, μ)-values for each panel are given in table 2.

	1		**2**	**3**	$\mathbf{H_o}$	$\mathbf{H_t}$
	$\mathbf{1_o}$	$\mathbf{1_t}$				
α	0.200	0.500	0.200	0.500	0.200	0.500
μ	0.050	0.001	−0.001	−0.002	0.000	0.000

Table 2: Representative parameter values for the open regions **1**–**3** and the homoclinic bifurcations $\mathbf{H_o}$ and $\mathbf{H_t}$, as used in fig. 7; all other parameter values are as in table 1.

4 Transition through the homoclinic bifurcations

In order to illustrate the difference between crossing the orientable homoclinic bifurcation $\mathbf{H_o}$ and the nonorientable homoclinic bifurcation $\mathbf{H_t}$ in fig. 5, we choose representative points in the regions **1** to **3** and at the bifurcations $\mathbf{H_t}$ and $\mathbf{H_o}$; see table 2 for the precise parameters chosen. In particular, we choose two points in region **1**, labelled $\mathbf{1_o}$ and $\mathbf{1_t}$, which are close to $\mathbf{H_o}$ and $\mathbf{H_t}$, respectively. The phase portraits with the respective global invariant objects in $\mathbb{R}^3$ are shown in fig. 7.

Region **1** is characterized by the existence of the orientable saddle periodic orbit Γ_o, the saddle equilibrium $\mathbf{0}$ and the stable-focus $\mathbf{q}$. Panel $\mathbf{1_o}$ of fig. 7 shows the corresponding phase portrait, which consists of the stable manifolds $W^s(\mathbf{0})$ (blue surface) and $W^s(\Gamma_o)$ (cyan surface), and the unstable manifolds $W^u(\mathbf{0})$ (red curve) and $W^u(\Gamma_t)$ (orange surface). Note that $W^s(\Gamma_o)$ is a topological cylinder that bounds the basin of attraction $\mathcal{B}(\mathbf{q})$ of $\mathbf{q}$. The manifold $W^s(\mathbf{0})$ accumulates from the outside onto $W^s(\Gamma_o)$ backward in time. One of the sheets that form $W^u(\Gamma_o)$ lies inside the topological cylinder $W^s(\Gamma_o)$ and, as such, it accumulates onto $\mathbf{q}$; the other sheet is bounded by $W^u(\mathbf{0})$. The accumulation of $W^s(\mathbf{0})$ onto $W^s(\Gamma_o)$ and the fact that $W^u(\mathbf{0})$ bounds one sheet of $W^u(\Gamma_o)$ are due to the λ-lemma [30, 40]: the existence of a nontransversal intersection between $W^s(\mathbf{0})$ and $W^u(\mathbf{0})$ implies the existence of a structurally stable heteroclinic orbit from Γ_o to $\mathbf{0}$. Notice that $W^u(\mathbf{0})$ spirals once around Γ_o before escaping to infinity, so that $\zeta = 1$ for this region. The boundary between regions $\mathbf{1_o}$ to **2** is the codimension-one orientable homoclinic bifurcation $\mathbf{H_o}$. At this bifurcation, the saddle periodic orbit Γ_o becomes the homoclinic orbit $\mathbf{\Gamma}_{\text{hom}}$ and the stable manifold $W^s(\mathbf{0})$ closes along its strong stable manifold $W^{ss}(\mathbf{0})$ in a topological cylinder; see panel $\mathbf{H_o}$ of fig. 7. However, the moment one transitions into region **2**, the homoclinic orbit $\mathbf{\Gamma}_{\text{hom}}$ disappears, allowing $W^u(\mathbf{0})$ to accumulate onto $\mathbf{q}$; see panel **2** of fig. 7. Hence, the ζ-value in this region is infinite.

We now focus on the transition through the codimension-one nonorientable homoclinic bifurcation $\mathbf{H_t}$. At the point $\mathbf{1_t}$, system eq. (1) is close to a nonorientable homoclinic bifurcation. Note that the computed manifolds in panels $\mathbf{1_t}$ and $\mathbf{1_o}$ are topologically equivalent, but the way $W^s(\mathbf{0})$ approaches backward in time onto $W^{ss}(\mathbf{0})$ vastly differs. In particular, note in panel $\mathbf{1_t}$ how the bottom part of the outer layer of $W^s(\mathbf{0})$ that accumulates onto $W^s(\Gamma_o)$ twists as it gets closer to $W^{ss}(\mathbf{0})$. In the transition from region $\mathbf{1_t}$ to region **3**, system eq. (1) exhibits the bifurcation $\mathbf{H_t}$ illustrated in panel $\mathbf{H_t}$ of fig. 7. At this bifurcation, the stable manifold $W^s(\mathbf{0})$ closes along its strong stable manifold $W^{ss}(\mathbf{0})$ in a topological Möbius band. In contrast to $\mathbf{H_o}$, the saddle periodic orbit Γ_o does not become the homoclinic orbit $\mathbf{\Gamma}_{\text{hom}}$ at the bifurcation $\mathbf{H_t}$. Then into region **3**, the saddle periodic orbit Γ_o persists and $\mathbf{\Gamma}_{\text{hom}}$ bifurcates into the nonorientable saddle periodic orbit Γ_t; see panel **3** of fig. 7. Its stable manifold $W^s(\Gamma_t)$ (purple surface) accumulates onto Γ_o backward in time, and $W^s(\mathbf{0})$ lies in between $W^s(\Gamma_o)$ and $W^s(\Gamma_t)$. Contrary to region **2**, the unstable manifold

$W^u(\mathbf{0})$ spirals twice around $W^s(\Gamma_o)$ and then escapes to infinity, so that $\zeta = 2$ for this region. Furthermore, the two-dimensional stable and unstable manifolds in region **3** have transverse intersections; in particular, we have a configuration of the form $\Gamma_o \to \Gamma_t \to \mathbf{0}$, that is, there exist heteroclinic orbits from Γ_o to Γ_t and from Γ_t to $\mathbf{0}$.

By applying the λ-lemma [30, 40] in a Poincaré section of Γ_t, we can show that $\Gamma_o \to \Gamma_t \to \mathbf{0}$ implies, in fact, the existence of infinitely many heteroclinic orbits from Γ_o to $\mathbf{0}$. Hence, we have the following:

Remark 4.1. *The phase portrait in region* **3** *is topological equivalent to that in region* **4** *for case* ***B*** *if we contract* Γ_o *to the point* $\mathbf{q}$*; see [12].*

4.1 Intersection sets with a sphere

fig. 8 shows the same series of phase portraits from fig. 7 in terms of intersection sets of the stable manifolds with the sphere $\mathbb{S}^* := \{x \in \mathbb{R}^3 : \| x - c \| = R\}$, where $c := (c_x, c_y, c_z) = (0.5, 0, 0)$ and $R = 0.6$; these intersection sets have been stereographically projected onto one of the tangent planes of $\mathbb{S}^*$. More precisely, we first apply the transformation

$$\pi = \left(\frac{u}{\| u \|}, \frac{v}{\| v \|}, \frac{w}{\| w \|} \right),$$

formed by the vectors

$$u = (0.5706, 0.1854, 0)^T, v = (1, -(u_x + u_z)/u_y, 1)^T \text{ and } w = u \times v.$$

We rotate and translate points $(x, y, z) \in \mathbb{S}^*$ to points (x', y', z') on the sphere of radius $R = 0.6$ centered at the origin, that is, $(x', y', z') = \pi(x - c)$. We then use stereographic projection from the south pole onto the tangent plane at the north pole, via the transformation

$$(x', y', z') \mapsto \left(\frac{Rx'}{R + z'}, \frac{Ry'}{R + z'} \right). \tag{3}$$

This particular stereographic projection was chosen to improve the visibility of certain features of the intersection sets specific to case **C**.

The left column of fig. 8 illustrates the transition through $\mathbf{H_o}$ and the right column through $\mathbf{H_t}$. Starting from panel $\mathbf{1_o}$ in fig. 8, note how the intersection set $\widehat{W}^s(\Gamma_o)$ (cyan curve) is made up of two topological circles that bound the disconnected basin $\widehat{\mathcal{B}}(\mathbf{q})$, that is, $\partial\widehat{\mathcal{B}}(\mathbf{q}) = \widehat{W}^s(\Gamma_o)$. The intersection $\widehat{W}^s(\mathbf{0})$ (blue curve) is a single curve that accumulates in a spiralling manner backward in time onto $\widehat{W}^s(\Gamma_o)$. The accumulation is as expected: the λ-lemma implies that the transversal heteroclinic orbit from Γ_o to $\mathbf{0}$ causes $\widehat{W}^s(\mathbf{0})$ to spiral around $\widehat{W}^s(\Gamma_o)$. Note that these phenomena are only observed if the sphere $\mathbb{S}^*$ is chosen small enough. At the moment of the bifurcation, shown in panel $\mathbf{H_o}$, the curve $\widehat{W}^s(\mathbf{0})$ closes back on itself along $\widehat{W}^{ss}(\mathbf{0})$ and $\widehat{W}^s(\Gamma_o)$ disappears as Γ_o becomes the homoclinic orbit Γ_{hom}; the basin $\widehat{\mathcal{B}}(\mathbf{q})$ is now bounded by a subset of $\widehat{W}^s(\mathbf{0})$, that is, $\partial\widehat{\mathcal{B}}(\mathbf{q}) \subset \widehat{W}^s(\mathbf{0})$. Hence, at $\mathbf{H_o}$, the boundary of the basin of attraction of $\mathbf{q}$ is contained in $W^s(\mathbf{0})$. As soon as we enter region **2**, the entire intersection set $\widehat{W}^s(\mathbf{0})$ becomes the boundary of $\widehat{\mathcal{B}}(\mathbf{q})$, which is now a connected region that is topologically equivalent to an open disk; see panel **2**.

In panel $\mathbf{1_t}$ of fig. 8, one sees the same topological configuration as in panel $\mathbf{1_o}$, because both phase portraits are from the same region; however, note how only one end of $\widehat{W}^s(\mathbf{0})$

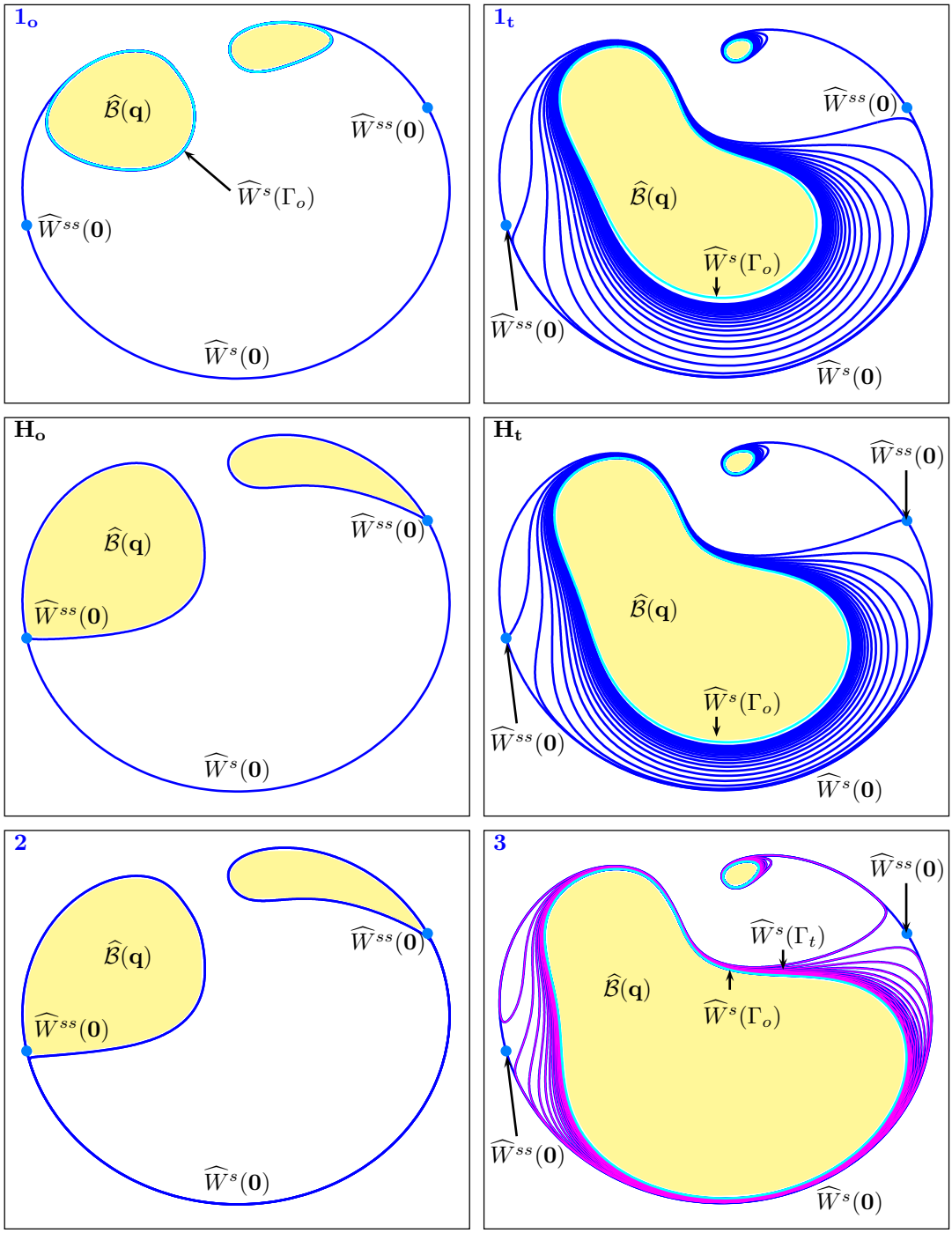

Figure 8: Stereographic projections of the intersection sets of the invariant manifolds with $\mathbb{S}^*$ in regions 1–3 and at the homoclinic bifurcations $\mathbf{H_o}$ and $\mathbf{H_t}$ near the inclination flip point $\mathbf{C_I}$. The left and right columns show the transition through the homoclinic bifurcations $\mathbf{H_o}$ and $\mathbf{H_t}$, respectively. Shown are $\widehat{W}^s(\mathbf{0})$ (dark-blue curves), $\widehat{W}^{ss}(\mathbf{0})$ (light-blue dots), $\widehat{W}^s(\Gamma_o)$ (cyan curve), $\widehat{W}^s(\Gamma_t)$ (purple curve) and $\widehat{\mathcal{B}}(\mathbf{q})$ (shaded yellow region). See table 2 for the respective parameter values.

gets close to both points in $\widehat{W}^{ss}(\mathbf{0})$ in panel $\mathbf{1_t}$. At the nonorientable homoclinic bifurcation $\mathbf{H_t}$, the intersection set $\widehat{W}^{s}(\mathbf{0})$ connects back on itself at $\widehat{W}^{ss}(\mathbf{0})$ in a different way, as is illustrated in panel $\mathbf{H_t}$ of fig. 8. Here, $\widehat{W}^{s}(\mathbf{0})$ does not bound two open regions as in panel $\mathbf{H_o}$. Instead, at $\mathbf{H_t}$ the two segments that form $\widehat{W}^{s}(\mathbf{0})$ accumulate onto the two topological circles $\widehat{W}^{s}(\Gamma_o)$ due to the persistence of the heteroclinic orbit from Γ_o to $\mathbf{0}$. The nature of $\widehat{\mathcal{B}}(\mathbf{q})$ and its boundary is unchanged from panel $\mathbf{1_o}$. As one transitions to region **3**, the homoclinic orbit $\mathbf{\Gamma}_{\text{hom}}$ becomes the periodic orbit Γ_t and the intersection set $\widehat{W}^{s}(\Gamma_t)$ (purple curve) is a single curve that accumulates at both ends onto $\widehat{W}^{s}(\Gamma_o)$ backward in time, due to the existence of a heteroclinic orbit from Γ_o to Γ_t. As mentioned before, there are infinitely many heteroclinic orbits from Γ_o to $\mathbf{0}$ in region **3**. Since $\mathbb{S}^*$ is a sufficiently small sphere that is transverse to $\widehat{W}^{s}(\mathbf{0})$, there exist infinitely many curves in $\widehat{W}^{s}(\mathbf{0})$. One curve in $\widehat{W}^{s}(\mathbf{0})$ accumulates onto a single topological circle of $\widehat{W}^{s}(\Gamma_o)$, and all other cuves accumulate onto both topological circles of $\widehat{W}^{s}(\Gamma_o)$. These sets of curves get arbitrary close to $\widehat{W}^{s}(\Gamma_t)$ from both sides; we say that $\widehat{W}^{s}(\Gamma_t)$ is a geometric accumulation curve of $\widehat{W}^{s}(\mathbf{0})$. In panel **3** of fig. 8 we only show three of these infinitely many intersection curves of $\widehat{W}^{s}(\mathbf{0})$, namely, the outer curve that accumulates onto the single topological circle of $\widehat{W}^{s}(\Gamma_o)$, and two other curves that track $\widehat{W}^{s}(\Gamma_t)$ on both sides. We remark that the intersection sets shown in fig. 8 are homotopic to the intersection sets shown in [12] for the transition through $\mathbf{H_o}$ and $\mathbf{H_t}$ in case **B**, provided one contracts $\widehat{W}^{ss}(\Gamma_o^a)$ to $\widehat{W}^{s}(\mathbf{q})$ through $\mathbf{H_o}$ and blows up $\widehat{W}^{s}(\mathbf{q})$ to a closed curve through $\mathbf{H_t}$ in case **B**.

The fact that $\Gamma_o \to \Gamma_t \to \mathbf{0}$ implies the existence of infinitely many structurally stable heteroclinic orbits from Γ_o to $\mathbf{0}$ is going to be a recurrent phenomenon for different equilibria and saddle periodic orbits. For ease of exposition, we summarize the consequences in general terms:

Proposition 4.2. *Let A, B and C be hyperbolic saddle equilibria or periodic orbits of system eq. (1). If $A \to B \to C$ then there exist infinitely many structurally stable orbits from A to C. Furthermore, if $W^s(A)$ intersects $\mathbb{S}^*$ transversally then there exist infinitely many curves in $\widehat{W}^{s}(C)$. Each curve in $\widehat{W}^{s}(C)$ accumulates onto $\widehat{W}^{s}(A)$ backward in time, and $\widehat{W}^{s}(B)$ is a geometric accumulation curve of $\widehat{W}^{s}(C)$.*

Proof. The proof follows from the λ-lemma and is a variation of the proof given in [12] for the case $\mathbf{q} \to \Gamma_t \to \mathbf{0}$. □

5 Cascades of homoclinic and heteroclinic bifurcations

We now focus our attention on the invariant manifolds of system eq. (1) during the cascades of homoclinic and heteroclinic bifurcations, which we study and illustrate along the line $\alpha = 0.5$ in the (α, μ)-plane.

5.1 Transition through $^2\mathbf{H_t}$

Starting from region **3**, we first encounter the codimension-one nonorientable homoclinic bifurcation $^2\mathbf{H_t}$ which is shown in fig. 9 as a stereographic projection of the stable invariant objects on $\mathbb{S}^*$ that exist in phase space. Panel (a) shows a sketch of the intersection sets in region **3** shown in fig. 8. The pink region indicates the relative location of the infinitely many curves in $\widehat{W}^{s}(\mathbf{0})$ that accumulate geometrically onto $\widehat{W}^{s}(\Gamma_t)$. At the moment of the

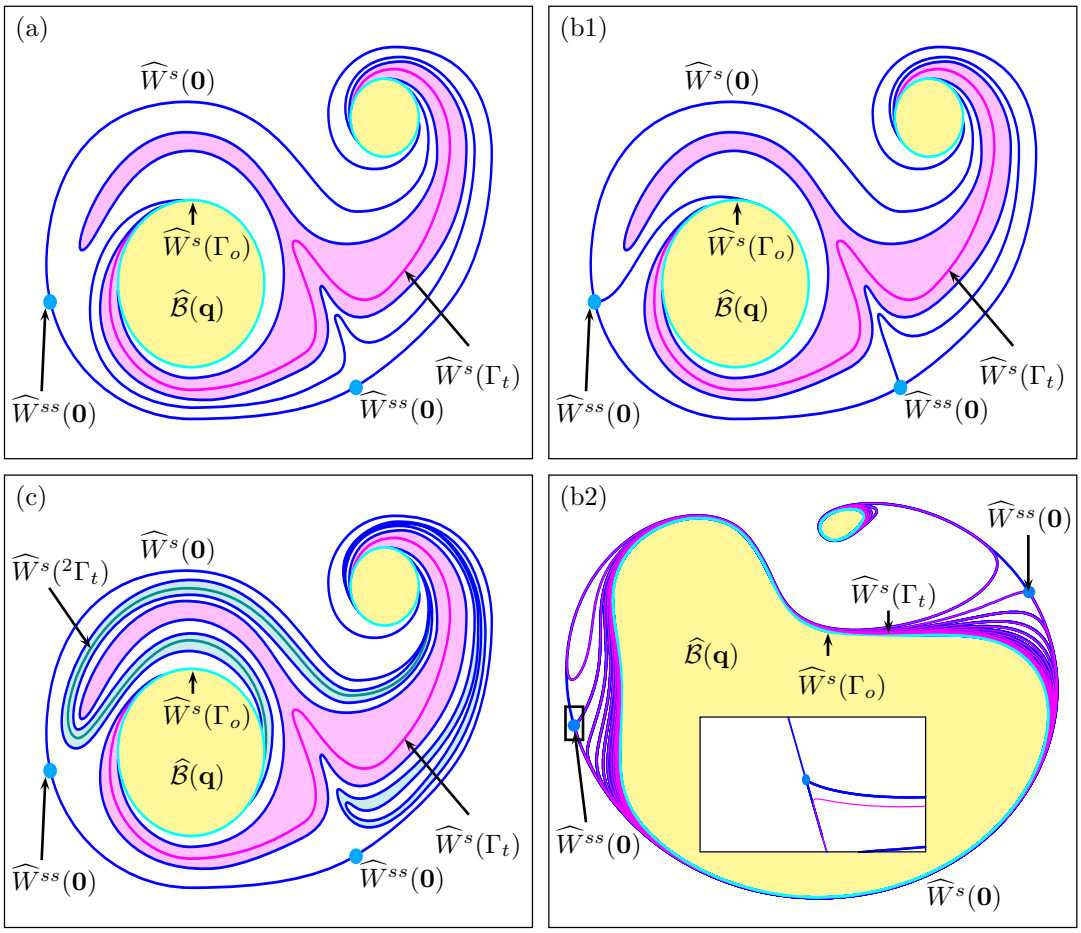

Figure 9: Stereographic projection of the intersection sets of the invariant manifolds with $\mathbb{S}^*$ before, at, and after the moment of the codimension-one homoclinic bifurcation $^{\mathbf{2}}\mathbf{H_t}$ in panels (a), (b1) and (b2), and (c), respectively. Panel (a) shows a sketch of the stereographic projection in region **3**; panels (b1) and (b2) show a sketch and the computed projections of system eq. (1) at $^{\mathbf{2}}\mathbf{H_t}$, respectively; and panel (c) shows a sketch after $^{\mathbf{2}}\mathbf{H_t}$. The color code and labeling of the regions is as in fig. 8. Panel (b2) is for parameter values $(\alpha, \mu) = (0.5, -0.002880267)$.

codimension-one homoclinic bifurcation ${}^2\mathbf{H_t}$, the outer-most curve in $\widehat{W}^s(\mathbf{0})$ that connects both topological circles of $\widehat{W}^s(\Gamma_o)$ split into two curves that close on $\widehat{W}^s(\mathbf{0})$ at the two points $\widehat{W}^{ss}(\mathbf{0})$; see the sketch in panel (b1) of fig. 9 and the associated computed phase portrait on $\mathbb{S}^*$ in panel (b2). The bifurcation ${}^2\mathbf{H_t}$ gives rise to the saddle periodic orbit ${}^2\Gamma_t$, and we find the following transversal connections: $\Gamma_o \to {}^2\Gamma_t \to \mathbf{0}$, $\Gamma_o \to \Gamma_t \to {}^2\Gamma_t$ and $\Gamma_o \to {}^2\Gamma_t \to \Gamma_t$. Panel (c) illustrates the situation by way of a representative sketch. Note how the two curves of $\widehat{W}^s(\mathbf{0})$ that end at $\widehat{W}^{ss}(\mathbf{0})$ in panel (b1) give rise to the two light-green regions, which represent the accumulation onto $\widehat{W}^s({}^2\Gamma_t)$ (dark-cyan curves) of infinitely many curves in $\widehat{W}^s(\mathbf{0})$ and $\widehat{W}^s(\Gamma_t)$ due to the existence of $\Gamma_o \to {}^2\Gamma_t \to \mathbf{0}$ and $\Gamma_o \to {}^2\Gamma_t \to \Gamma_t$; we refer to proposition 4.2. Both circles in $\widehat{W}^s(\Gamma_o)$ bound one of these two regions, but only one circle in $\widehat{W}^s(\Gamma_o)$ bounds the other region. Furthermore, since $\Gamma_o \to \Gamma_t \to \mathbf{0}$ and $\Gamma_o \to \Gamma_t \to {}^2\Gamma_t$, the pink region must contain infinitely many curves of $\widehat{W}^s({}^2\Gamma_t)$, and infinitely many curves in $\widehat{W}^s(\mathbf{0})$ also accumulate geometrically onto these curves. The existence of both pink and light-green regions is important. As μ decreases, the outer-most curve from the region that is closest to $\widehat{W}^{ss}(\mathbf{0})$ will meet $\widehat{W}^{ss}(\mathbf{0})$ at a certain value μ^*; depending on whether this is a curve from $\widehat{W}^s(\mathbf{0})$, $\widehat{W}^s(\Gamma_t)$ or $\widehat{W}^s({}^2\Gamma_t)$, system eq. (1) exhibits a particular corresponding codimension-one homoclinic or heteroclinic bifurcation. Furthermore, as the infinitely many curves in $\widehat{W}^s(\mathbf{0})$ accumulate onto either $\widehat{W}^s(\Gamma_t)$ or $\widehat{W}^s({}^2\Gamma_t)$, infinitely many homoclinic bifurcations must occur before a codimension-one heteroclinic bifurcation can take place. Whenever a homoclinic bifurcation occurs, the above sequence of different kinds of bifurcations occurs again; that is, an additional saddle periodic orbit is created, accompanied by two regions of accumulation with respect to the stable manifold of the new saddle periodic orbit. Moreover, an accumulation of intersection curves from this stable manifold is created inside the already existing regions. In addition, the closer $\widehat{W}^s(\mathbf{0})$ lies to $\widehat{W}^s(\Gamma_t)$ or $\widehat{W}^s({}^2\Gamma_t)$, the higher the number of rotations are for both the homoclinic orbit and the bifurcating saddle periodic orbit.

5.2 Transition through $\mathbf{Q_0^{\Gamma_t}}[\Gamma_o]$

We illustrate in fig. 10 the transition through the codimension-one heteroclinic bifurcation $\mathbf{Q_0^{\Gamma_t}}[\Gamma_o]$ and its effect on the reorganization of the stable manifold $W^s(\Gamma_t)$ (purple surface) in phase space. The left column shows $W^s(\Gamma_t)$ in a tubular neighborhood of Γ_t, showing that $W^s(\Gamma_t)$ is topologically a Möbius band. The right column (2) shows a larger part of $W^s(\Gamma_t)$. Panels (a1) and (a2) show $W^s(\Gamma_t)$, at $\mu = -0.002$, before the bifurcation $\mathbf{Q_0^{\Gamma_t}}[\Gamma_o]$ and the associated first homoclinic cascade; panels (b1) and (b2) are at the moment of the bifurcation, when $\mu \approx -0.002880324$; and panels (a3) and (b3) are for $\mu = -0.0035$, in region 4 past the first cascade; see fig. 5.

We first focus on the local behavior in a tubular neighborhood. In panel (a1), the unstable manifold $W^u(\mathbf{0})$ (red curve) makes one rotation close to Γ_o and one close to Γ_t and then escapes to infinity. As discussed before, a sequence of homoclinic bifurcations must occur before the bifurcation $\mathbf{Q_0^{\Gamma_t}}[\Gamma_o]$ is exhibited by system eq. (1). During this sequence, the unstable manifold $W^u(\mathbf{0})$ gains turns around $W^s(\Gamma_t)$, thus increasing ζ, until its limiting case at the bifurcation $\mathbf{Q_0^{\Gamma_t}}[\Gamma_o]$. However, note how the first loop of $W^u(\mathbf{0})$ is still close to Γ_o before accumulating onto Γ_t; this situation is the same as in panel (a1) of fig. 6. After $\mathbf{Q_0^{\Gamma_t}}[\Gamma_o]$, a sequence of homoclinic bifurcations occur which decreases the winding number of $W^u(\mathbf{0})$ around $W^s(\Gamma_t)$, thus decreasing ζ. Finally in region 4, the unstable manifold $W^u(\mathbf{0})$ makes two rotation close to Γ_o and one again close to Γ_t before escaping to infinity; see

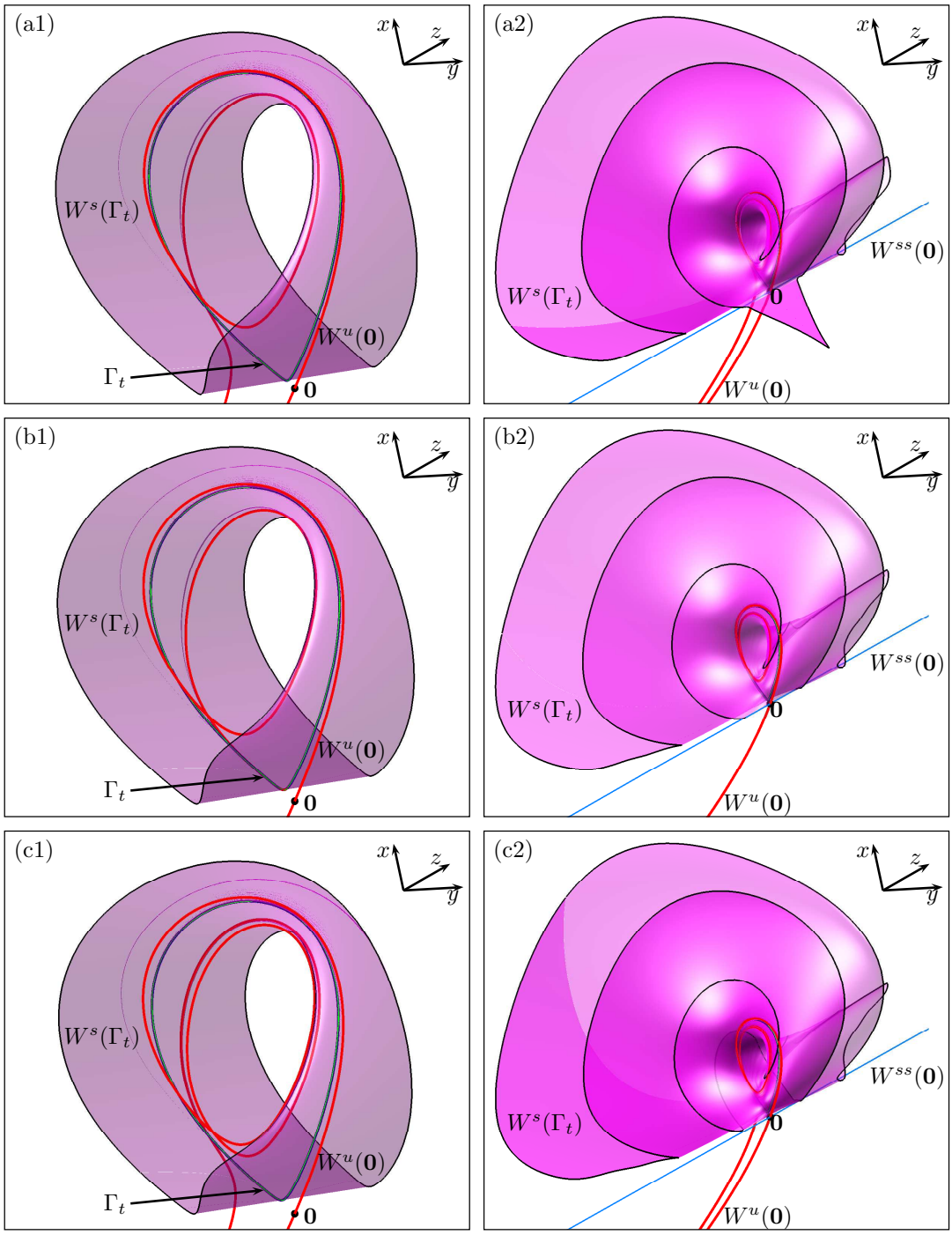

Figure 10: The stable manifold $W^s(\Gamma_t)$ (purple surface) of the nonorientable saddle periodic orbit Γ_t (green curve), together with $W^u(\mathbf{0})$ (red curve) and $W^{ss}(\mathbf{0})$ (blue curve) before, at, and after the moment of the codimension-one heteroclinic bifurcation $\mathbf{Q}_{\mathbf{0}}^{\Gamma_t}[\Gamma_o]$ of system eq. (1) in rows (a), (b) and (c), respectively. The left column shows $W^s(\Gamma_t)$ in a tubular neighborhood of Γ_t, and the right column shows a larger part of $W^s(\Gamma_t)$. Rows (a), (b) and (c) are for $(\alpha, \mu) = (0.5, -0.002)$, $(\alpha, \mu) = (0.5, -0.002880324)$ and $(\alpha, \mu) = (0.5, -0.0035)$, respectively.

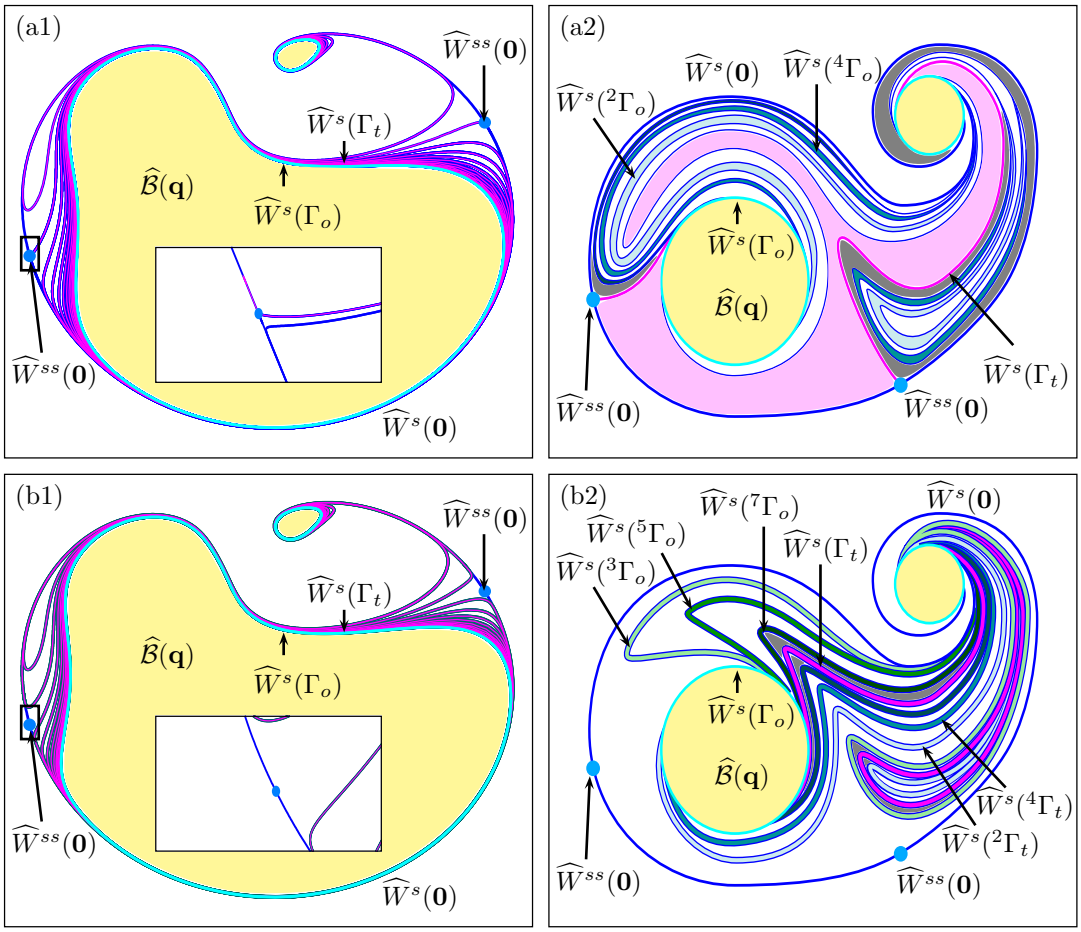

Figure 11: Stereographic projection of the intersection sets of the invariant manifolds with $\mathbb{S}^*$ at the codimension-one heteroclinic bifurcation $\mathbf{Q}_{\mathbf{0}}^{\Gamma_t}$, in region 4, and at the codimension-one heteroclinic bifurcation $\mathbf{Q}_{\mathbf{0}}^{\Gamma_o}$ in rows (a) and (b), respectively. The left column shows the computed projections and the right column corresponding sketches. The color code and labeling of the regions is the same as in fig. 8. Panels (a1), and (b1) are for $(\alpha, \mu) = (0.5, -0.002880324)$ and $(\alpha, \mu) = (0.5, -0.0035)$, respectively.

panel (c1). In particular, the orientation of the homoclinic bifurcation of $\mathbf{0}$ that follows, depends on how $W^u(\mathbf{0})$ passes near Γ_o and Γ_t.

We gain a deeper understanding by studying a larger portion of $W^s(\Gamma_t)$ as shown in the right column of fig. 10. Panel (a2) illustrates how $W^s(\Gamma_t)$ spirals around $W^s(\Gamma_o)$ due to the presence of heteroclinic orbits from Γ_o to Γ_t; the outer rim of the computed part of $W^s(\Gamma_t)$ is highlighted as the black curve. Note how part of $W^s(\Gamma_t)$ gets close to $W^{ss}(\mathbf{0})$ before starting to spiral again. In panel (b2), this part of $W^s(\Gamma_t)$ has disappeared, and the existence of the heteroclinic orbit $\mathbf{Q}_{\mathbf{0}}^{\Gamma_t}[\Gamma_o]$ forces $W^s(\Gamma_t)$ to accumulate onto $W^{ss}(\mathbf{0})$ backward in time. After the bifurcation $\mathbf{Q}_{\mathbf{0}}^{\Gamma_t}[\Gamma_o]$, the manifold $W^s(\Gamma_t)$ no longer accumulates onto $W^{ss}(\mathbf{0})$; see panel (c2). Observe that $W^s(\Gamma_t)$ in panel (c2) seems identical to $W^s(\Gamma_t)$ in panel (b2), but it exhibits one additional loop. This extra loop would spread out if a much larger portion of $W^s(\Gamma_t)$ were computed, and it would get close to $W^{ss}(\mathbf{0})$ in the same way as in panel (a2).

Figure 11 illustrates the transition to region 4 on the level of the intersection sets of the invariant objects with $\mathbb{S}^*$. Panels (a1) and (a2) are stereographic projections of the intersection sets with $\mathbb{S}^*$ at the moment of the first codimension-one heteroclinic bifurcation $\mathbf{Q}_{\mathbf{0}}^{\Gamma_t}[\Gamma_o]$ of Γ_t. At the moment of the bifurcation the curve $\widehat{W}^s(\Gamma_t)$ (purple) splits into two

curves that meet at the two points in $\widehat{W}^{ss}(\mathbf{0})$; see panel (a1). This phenomenon is illustrated more clearly in the sketch shown in panel (a2), where the accumulation of curves in $\widehat{W}^{s}(\Gamma_t)$ is represented by the pink shading. As mentioned before, each homoclinic bifurcation creates a saddle periodic orbit that gives rise to two new accumulation regions in the intersection set with $\mathbb{S}^*$; these are shaded in panel (a2) with different tones of cyan and the label indicates the intersection curve of the principal stable manifold. Only two pairs of accumulation regions are indicated in panel (a2). The gray region represents the infinitely many regions created in further homoclinic bifurcations and specifies their relative location in the stereographic projection. It is clear from panels (a1) and (a2) of fig. 11 that, after crossing of $\mathbf{Q}_{\mathbf{0}}^{\Gamma_t}[\Gamma_o]$, there is another cascade of homoclinic bifurcations that terminates on the homoclinic bifurcation associated with the blue curve in $\widehat{W}^{s}(\mathbf{0})$ that bounds the pink region in panel (a2); this last homoclinic bifurcation corresponds to the last bifurcation that system eq. (1) exhibits before transitioning into region **4** in fig. 5. Panels (b1) and (b2) in fig. 11 show the situation in region 4 on the level of the stereographic projections. In particular, each accumulation region is represented by the main intersection curve of the stable manifold of the saddle periodic orbit that exists on it. Observe how one of the curves of $\widehat{W}^{s}(\Gamma_t)$ and, thus, the corresponding accumulation region accumulate onto a single topological circle of $\widehat{W}^{s}(\Gamma_o)$, while the other curve accumulates on both topological circles of $\widehat{W}^{s}(\Gamma_o)$. This is true for each of the accumulation regions of the different saddle periodic orbits, while they accumulate at the same time onto $\widehat{W}^{s}(\Gamma_t)$ (gray region).

5.3 Transition through $\mathbf{Q}_{\mathbf{0}}^{\Gamma_o}$

The final step at the end of all cascades is the heteroclinic bifurcation $\mathbf{Q}_{\mathbf{0}}^{\Gamma_o}$. The two-dimensional stable manifold $W^{s}(\Gamma_o)$ does not interact with any saddle invariant object, and it retains its topological properties during the cascades of homoclinic and heteroclinic bifurcations. However, this changes as soon as $W^{s}(\Gamma_o)$ intersects $W^{u}(\mathbf{0})$ at the bifurcation $\mathbf{Q}_{\mathbf{0}}^{\Gamma_o}$, which is illustrated in fig. 12. Specifically, the left column shows $W^{s}(\Gamma_o)$ (cyan surface), together with $W^{u}(\mathbf{0})$ (red curve), in a tubular neighborhood of Γ_o and the right column shows larger parts of these manifolds. Panels (a1) and (a2) show, at $\mu = -0.002$, the situation before the bifurcation $\mathbf{Q}_{\mathbf{0}}^{\Gamma_o}$, that is, during the homoclinic and heteroclinic cascades; panels (b1) and (b2) are for $\mu \approx -0.004861805$ at the moment of the bifurcation $\mathbf{Q}_{\mathbf{0}}^{\Gamma_o}$; and panels (a3) and (b3) are for $\mu = -0.005$, after the bifurcation. It seems that, in the vicinity of Γ_o, the transition through $\mathbf{Q}_{\mathbf{0}}^{\Gamma_o}$ does not manifest itself as any topological change for $W^{s}(\Gamma_o)$, apart from its relative position with respect to $W^{u}(\mathbf{0})$. Hence, in panels (a1), (b1) and (c1), one sees $W^{u}(\mathbf{0})$ outside, at, and inside the topological cylinder $W^{s}(\Gamma_o)$, respectively. The difference becomes apparent only when we consider a larger portion of phase space. In panel (a2), the stable manifold $W^{s}(\Gamma_o)$ is still a topological cylinder, but note how part of $W^{s}(\Gamma_o)$ lies close to $W^{ss}(\mathbf{0})$. The moment $\mathbf{Q}_{\mathbf{0}}^{\Gamma_o}$ occurs, in panel (b2), one trajectory of the unstable manifold manifold $W^{u}(\mathbf{0})$ lies inside $W^{s}(\Gamma_o)$ which forces $W^{s}(\Gamma_o)$ to accumulate onto $W^{ss}(\mathbf{0})$ backward in time. After the bifurcation $\mathbf{Q}_{\mathbf{0}}^{\Gamma_o}$, as shown in panel (c2) of fig. 12, the lower half of $W^{s}(\Gamma_o)$ starts to spiral around its upper half. The spiralling accumulation is due to the existence of structurally stable homoclinic orbits of Γ_o. Note in panel (c2) that one branch of $W^{u}(\mathbf{0})$ lies in the basin $\mathcal{B}(\mathbf{q})$ and the other one lies in the positive invariant set V, as defined in section 2.2. Hence, the winding number ζ is infinite and there cannot be any homoclinic or heteroclinic bifurcations occurring after $\mathbf{Q}_{\mathbf{0}}^{\Gamma_o}$. This implies that $\mathbf{Q}_{\mathbf{0}}^{\Gamma_o}$ marks the end of the homoclinic and heteroclinic cascade in the (α, μ)-plane.

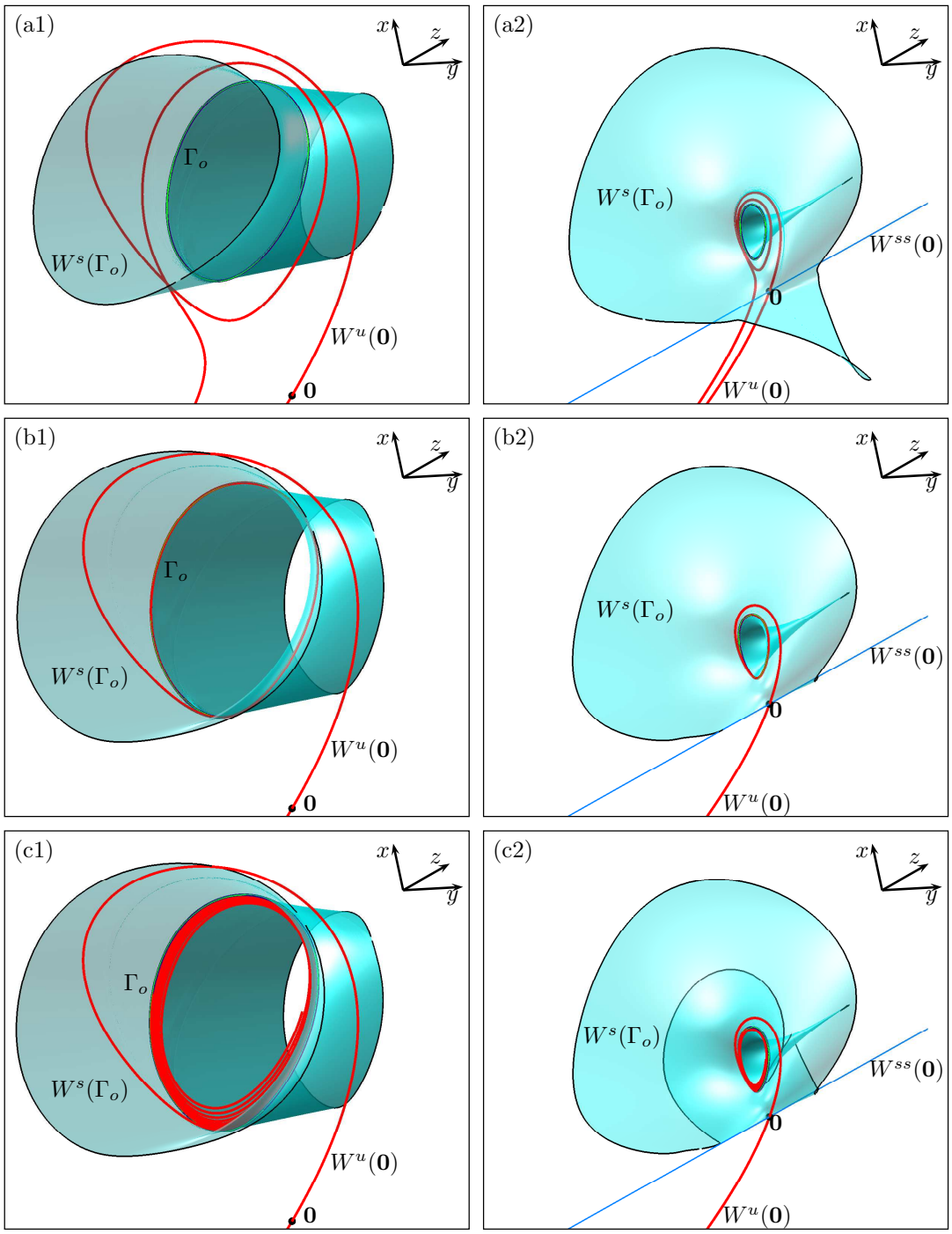

Figure 12: The stable manifold $W^s(\Gamma_o)$ (cyan surface) of the orientable saddle periodic orbit Γ_o (purple curve), together with $W^u(\mathbf{0})$ (red curve) and $W^{ss}(\mathbf{0})$ before, at, and after the moment of the codimension-one heteroclinic bifurcation $\mathbf{Q}_{\mathbf{0}}^{\Gamma_o}$ of system eq. (1) in rows (a), (b) and (c), respectively. The left column shows $W^s(\Gamma_t)$ in a tubular neighborhood of Γ_t, and the right column shows a larger part of $W^s(\Gamma_t)$. Rows (a), (b) and (c) are for $(\alpha, \mu) = (0.5, -0.002)$, $(\alpha, \mu) = (0.5, -0.004861805)$ and $(\alpha, \mu) = (0.5, -0.005)$, respectively.

5.4 Computation of bifurcation sequences

To determine different homoclinic and heteroclinic cascades, and to understand their organization in the parameter plane, we computed representative bifurcation points and their corresponding μ-values along the line $\alpha = 0.5$. These are listed in table 3, which also lists the sequence of further bifurcations past these cascades. We first discuss the global bifurcations up to $\mathbf{Q_0^{\Gamma_o}}$ and then the remaining bifurcations.

As μ decreases from the primary homoclinic bifurcation $\mathbf{H_t}$ at $\mu = 0$, we encounter homoclinic and heteroclinic cascades in a particular order, followed by saddle-node and period-doubling bifurcations of periodic orbits. As mentioned before, a saddle periodic orbit is created for each homoclinic bifurcation that occurs as μ decreases; e.g., the saddle periodic orbits Γ_t and ${}^2\Gamma_t$ are created from the homoclinic bifurcations $\mathbf{H_t}$ and $\mathbf{{}^2H_t}$, respectively. We now employ a similar notation as used for the heteroclinic bifurcations to denote the subsequent homoclinic bifurcations where the corresponding orbit makes rotations around certain saddle periodic orbits before accumulating backward and forward in time to $\mathbf{0}$. For ease of exposition, we append this information in their corresponding labels. For example, $\mathbf{H_o}[n\Gamma_o, m\Gamma_t]$ represents the codimension-one orientable homoclinic bifurcation where the corresponding orbit makes n turns around Γ_o and then m turns around Γ_t before accumulating forward in time to $\mathbf{0}$. In particular, the homoclinic bifurcations $\mathbf{H_o}[n\Gamma_o, m\Gamma_t]$ or $\mathbf{H_t}[n\Gamma_o, m\Gamma_t]$, for $n, m \in \mathbb{N}$, in table 3 create saddle periodic orbits that make $n + m + 1$ loops (the first rotation cannot be assigned to any saddle periodic orbit) and have the same orientation as the homoclinic bifurcation. Heuristically, one can get information about the orientation of the homoclinic bifurcation by looking at the parity of m, that is, the amount of times the corresponding orbit of the homoclinic bifurcation rotates around Γ_t in phase space before converging to $\mathbf{0}$. In general the first turn changes the orientation of the homoclinic bifurcation to nonorientable, and every time a rotation occurs around Γ_t, the orientation swaps; hence, for odd m the corresponding bifurcation is nonorientable and for even m it is orientable. For example, observe in table 3 that the homoclinic cascade of the form $\mathbf{H_t}[\Gamma_o, m\Gamma_t]$, with m even, increases in the number of rotations around Γ_t until it accumulates onto $\mathbf{Q_0^{\Gamma_t}}[\Gamma_o]$; the number of rotations then starts decreasing, with m odd, up to $\mathbf{H_o}[\Gamma_o, \Gamma_t]$. In particular, $\mathbf{H_o}[\Gamma_o, \Gamma_t]$ is the last bifurcation that occurs before transitioning into region 4. Note that between $\mathbf{H_o}[\Gamma_o, \Gamma_t]$ and $\mathbf{H_t}[2\Gamma_o]$ there is a larger gap in μ compared to the previous homoclinic bifurcations. This is due to the termination and the start of new homoclinic and heteroclinic cascades, respectively. In particular, these two homoclinic bifurcations are related as they create the saddle periodic orbits ${}^3\Gamma_o$ and ${}^3\Gamma_t$, which disappear in the saddle-node bifurcation $\mathbf{SNP}_{{}^3\Gamma_o}$. Because ζ remains constant at $\zeta = 3$, we also have numerical evidence that during this gap there cannot exist additional homoclinic or heteroclinic bifurcations.

We also present in table 3 the μ-values of representative codimension-one heteroclinic bifurcations from $\mathbf{0}$ to ${}^2\Gamma_t$. For example, at the heteroclinic bifurcation $\mathbf{Q_0^{{}^2\Gamma_t}}[2\Gamma_o]$, system eq. (1) exhibits a heteroclinic orbit that connects $\mathbf{0}$ to ${}^2\Gamma_t$ while rotating twice around Γ_o. This shows that there exist additional cascades inside the cascade $\mathbf{H_o}[2\Gamma_o, m\Gamma_t]$ with m even, and the same holds for the cascade $\mathbf{H_t}[2\Gamma_o, m\Gamma_t]$ with m odd, as our topological sketch in panel (b2) of fig. 11 suggests due to the λ-lemma. In general, there must be cascades of the form $\mathbf{H_{o/t}}[2\Gamma_o, m\Gamma^*]$, $m \in \mathbb{N}$, where Γ^* is a different saddle periodic orbit, accumulating onto heteroclinic bifurcations $\mathbf{Q_0^{\Gamma^*}}[2\Gamma_o]$. Therefore, there exist entire clusters of cascades. These clusters of cascades are repeated starting from $\mathbf{H_t}[2\Gamma_o]$ and ending at $\mathbf{H_o}[2\Gamma_o, \Gamma_t]$, and again for the pair $\mathbf{H_t}[3\Gamma_o]$ and $\mathbf{H_o}[3\Gamma_o, \Gamma_t]$, and so on. In general, the center of each cluster corresponds to the heteroclinic bifurcation $\mathbf{Q_0^{\Gamma_t}}[n\Gamma_o]$, with $n = 2, 3, 4, 5, ...$, which occurs only once

Bifurcation	$\mu \times [10^{-3}]$
$\mathbf{H_t}$	0.0
$\mathbf{^2H_t}$	-2.880268
$\mathbf{H_t}[\Gamma_o, 2\Gamma_t]$	-2.880324
$\mathbf{H_t}[\Gamma_o, 4\Gamma_t]$	-2.880324
$\mathbf{H_t}[\Gamma_o, 6\Gamma_t]$	-2.880324
$\mathbf{H_t}[\Gamma_o, 8\Gamma_t]$	-2.880324
$\mathbf{Q_0^{\Gamma_t}}[\Gamma_o]$	-2.880324
$\mathbf{H_o}[\Gamma_o, 7\Gamma_t]$	-2.880324
$\mathbf{H_o}[\Gamma_o, 5\Gamma_t]$	-2.880324
$\mathbf{H_o}[\Gamma_o, 3\Gamma_t]$	-2.880324
$\mathbf{H_o}[\Gamma_o, \Gamma_t]$	-2.880325
$\mathbf{H_t}[2\Gamma_o]$	-3.816057
$\mathbf{Q_0^{^2\Gamma_t}}[2\Gamma_o]$	-3.816058
$\mathbf{Q_0^{\Gamma_t}}[2\Gamma_o]$	-3.816233
$\mathbf{Q_0^{^2\Gamma_t}}[2\Gamma_o, \Gamma_t]$	-3.816233
$\mathbf{H_o}[2\Gamma_o, \Gamma_t]$	-3.816234
$\mathbf{H_t}[3\Gamma_o]$	-4.249463
$\mathbf{Q_0^{^2\Gamma_t}}[3\Gamma_o]$	-4.249465
$\mathbf{Q_0^{\Gamma_t}}[3\Gamma_o]$	-4.249668
$\mathbf{Q_0^{^2\Gamma_t}}[3\Gamma_o, \Gamma_t]$	-4.249669
$\mathbf{H_o}[3\Gamma_o, \Gamma_t]$	-4.249669
$\mathbf{H_t}[4\Gamma_o]$	-4.483178
$\mathbf{Q_0^{^2\Gamma_t}}[4\Gamma_o]$	-4.483183
$\mathbf{Q_0^{\Gamma_t}}[4\Gamma_o]$	-4.483359
$\mathbf{Q_0^{^2\Gamma_t}}[4\Gamma_o, \Gamma_t]$	-4.483360
$\mathbf{H_o}[4\Gamma_o, \Gamma_t]$	-4.483359

Bifurcation	$\mu \times [10^{-3}]$
$\mathbf{H_t}[5\Gamma_o]$	-4.619987
$\mathbf{Q_0^{^2\Gamma_t}}[5\Gamma_o]$	-4.619993
$\mathbf{Q_0^{\Gamma_t}}[5\Gamma_o]$	-4.620120
$\mathbf{H_o}[5\Gamma_o, \Gamma_t]$	-4.620128
$\mathbf{H_t}[6\Gamma_o]$	-4.704132
$\mathbf{H_o}[6\Gamma_o, \Gamma_t]$	-4.704235
$\mathbf{H_t}[7\Gamma_o]$	-4.757563
$\mathbf{H_o}[7\Gamma_o, \Gamma_t]$	-4.757636
$\mathbf{H_t}[8\Gamma_o]$	-4.792227
$\mathbf{H_o}[8\Gamma_o, \Gamma_t]$	-4.792278
$\mathbf{H_t}[9\Gamma_o]$	-4.815051
$\mathbf{Q_0^{\Gamma_o}}$	-4.861805
$\mathbf{F}$	-7.054355
$\mathbf{Tan}_{\Gamma_o}$	-7.076705
$\mathbf{SNP}_{10\Gamma_o}$	-7.077572
$\mathbf{SNP}_{9\Gamma_o}$	-7.078122
$\mathbf{SNP}_{7\Gamma_o}$	-7.080554
$\mathbf{SNP}_{6\Gamma_o}$	-7.083202
$\mathbf{SNP}_{5\Gamma_o}$	-7.088049
$\mathbf{SNP}_{4\Gamma_o}$	-7.097747
$\mathbf{SNP}_{3\Gamma_o}$	-7.120570
$\mathbf{PD}_{8\Gamma_t}$	-7.151054
$\mathbf{PD}_{4\Gamma_t}$	-7.153300
$\mathbf{PD}_{2\Gamma_t}$	-7.163762
$\mathbf{PD}_{\Gamma_t}$	-7.211185
$\mathbf{SNP}_{\Gamma_o}$	-7.386406

Table 3: Computed μ-values at a selection from the infinitely many bifurcations points along the slice $\alpha = 0.5$ of system eq. (1). The color of each bifurcation point matches the corresponding curve in fig. 5. We also show the heteroclinic bifurcation $\mathbf{Q_0^{^2\Gamma_t}}$ from $\mathbf{0}$ to $^2\Gamma_t$ (gray). The ordering and clustering of these bifurcations is illustrated in fig. 13.

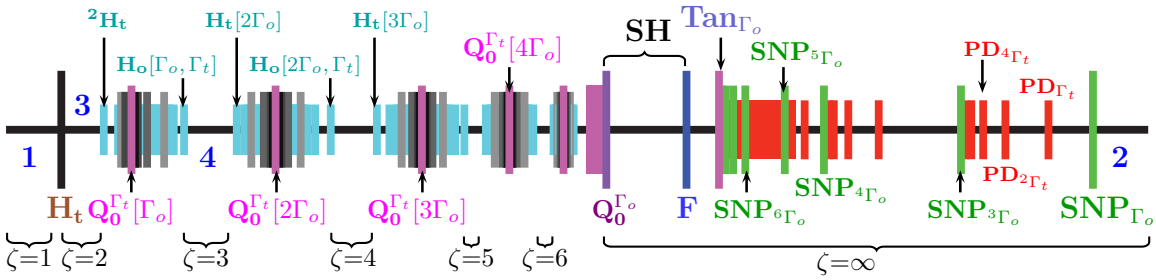

Figure 13: Sketch of the bifurcation sequence along the slice $\alpha = 0.5$ for the bifurcation diagram of system eq. (1) in fig. 5. Here, μ decreases to the right; see also table 3.

in each cluster. For example, note from table 3 that the heteroclinic bifurcation $\mathbf{Q_0^{\Gamma_t}}[2\Gamma_o]$ lies in between the bifurcations $\mathbf{Q_0^{^2\Gamma_t}}[2\Gamma_o]$ and $\mathbf{Q_0^{^2\Gamma_t}}[2\Gamma_o,\Gamma_t]$. Furthermore, the last orientable homoclinic bifurcation from the second cluster, i.e., $\mathbf{H_o}[2\Gamma_o,\Gamma_t]$, is associated with the first nonorientable homoclinic bifurcation in the second cluster, i.e. $\mathbf{H_t}[3\Gamma_o]$, because they create the saddle periodic orbits $^4\Gamma_o$ and $^4\Gamma_t$ that disappear in the saddle-node bifurcation $\mathbf{SNP}_{^4\Gamma_o}$. These two homoclinic bifurcations also form a big region in the bifurcation diagram fig. 5 with $\zeta = 4$ constant. After $\mathbf{H_o}[2\Gamma_o,\Gamma_t]$ occurs, the rotation of $W^u(\mathbf{0})$ around Γ_t moves closer to Γ_o as μ decreases, until it becomes $\mathbf{H_t}[3\Gamma_o]$. Similarly, the third cluster of cascades ends with the orientable homoclinic bifurcation $\mathbf{H_o}[3\Gamma_o,\Gamma_t]$, which is associated with the first homoclinic bifurcation $\mathbf{H_t}[4\Gamma_o]$, because they create $^5\Gamma_o$ and $^5\Gamma_t$ which disappear in $\mathbf{SNP}_{^5\Gamma_o}$; these two homoclinic bifurcations also form a big region in the bifurcation diagram fig. 5, now with $\zeta = 5$. In general, the last orientable homoclinic bifurcation of a cluster and the first nonorientable homoclinic bifurcation in the following cluster of cascades bound a big region in the bifurcation diagram fig. 5 with the number of their loops corresponding to the value of ζ. We are able to compute the homoclinic clusters up to $\mathbf{H_o}[8\Gamma_o,\Gamma_t]$ and $\mathbf{H_t}[9\Gamma_o]$, and detect the heteroclinic bifurcations up to $\mathbf{Q_0^{\Gamma_t}}[5\Gamma_o]$. The cascade ends on $\mathbf{Q_0^{\Gamma_o}}$, which marks the start, as μ decreases, of a regime with transversal homoclinic orbits of Γ_o, that is, the existence of Smale–horseshoe dynamics [31].

5.5 Graphical representation of the bifurcation sequence

Figure 13 presents a sketch of the bifurcation sequence along the slice $\alpha = 0.5$ from table 3. Here, we illustrate how the infinitely many homoclinic and heteroclinic bifurcations organize themselves according to our discussion in the previous paragraph. The intersection sets presented in fig. 11 give us a good explanation for the gap between $\mathbf{H_o}[\Gamma_o,\Gamma_t]$ and $\mathbf{H_t}[2\Gamma_o]$ in fig. 13 and the corresponding gap between the μ-values in table 3: the curves in $\widehat{W}^s(\mathbf{0})$ involved in these two bifurcations are the boundaries of their respective clusters of accumulation, which are locally isolated. Notice that this is the case for all pairs of homoclinic bifurcations $\mathbf{H_o}[m\Gamma_o,\Gamma_t]$ and $\mathbf{H_t}[(m+1)\Gamma_o]$, as found for $m = 1,2,3,4,5,6,7,8,9$ in table 3. Furthermore, each gap provides a parameter window during which the extra loop of $W^u(\mathbf{0})$, created in the respective codimension-one heteroclinic bifurcation $\mathbf{Q_0^{\Gamma_t}}$, moves closer to Γ_o; recall that the next homoclinic bifurcation of Γ_o will be nonorientable. During these gaps, the value of the winding number ζ remains constant and is given by the number of loops of the homoclinic orbits that bound the region in (α,μ)-plane. Note that after every cluster of accumulation, the unstable manifold $W^u(\mathbf{0})$ gains a rotation that lies closer to Γ_o. This mean that, as μ decreases, the ζ value in each gap increases until it reaches infinity at $\mathbf{Q_0^{\Gamma_o}}$.

Figure 13 also illustrates the order of further bifurcations past $\mathbf{Q_0^{\Gamma_o}}$ that are computed

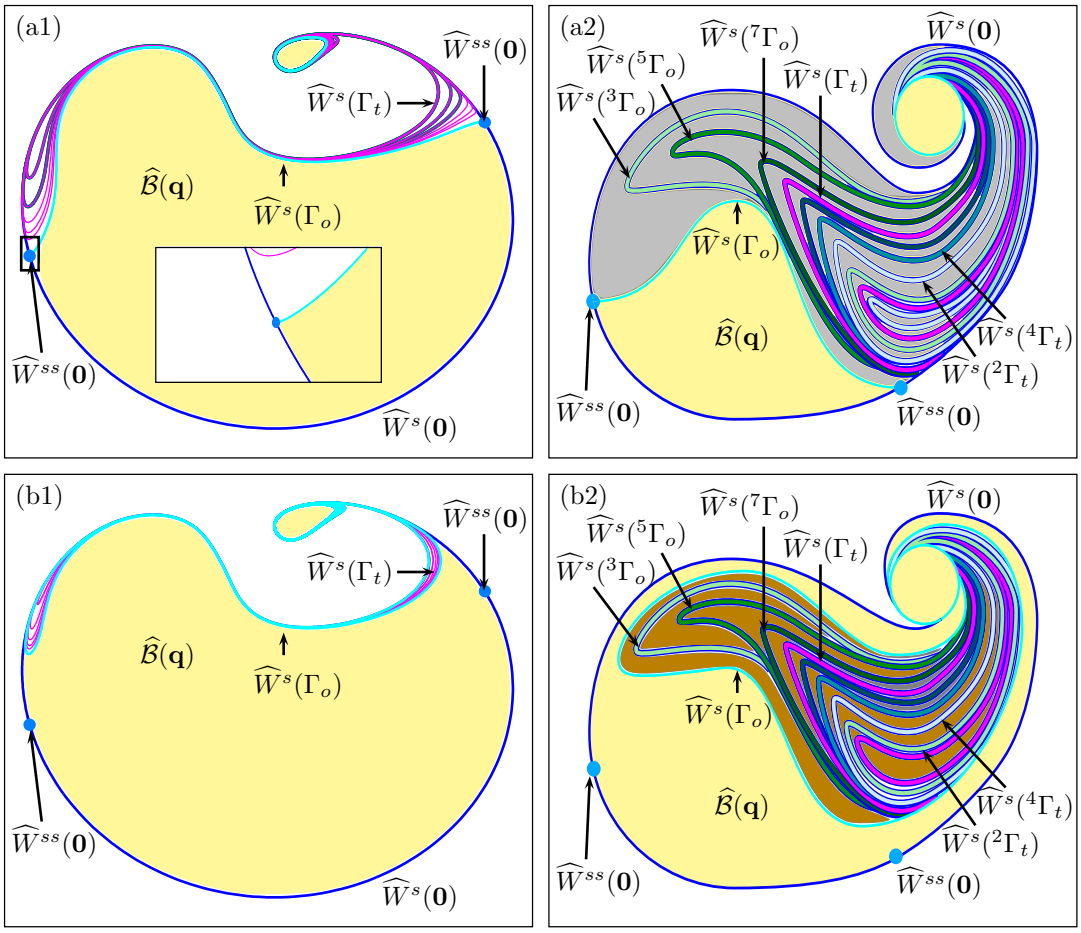

Figure 14: Stereographic projection of the intersection sets of the invariant manifolds with $\mathbb{S}^*$ at, and after the codimension-one heteroclinic bifurcation $\mathbf{Q}_{\mathbf{0}}^{\Gamma_o}$ in rows (a) and (b), respectively. Column (1) shows the computed projections and column (2) shows corresponding sketches. The color code and labeling of the regions is the same as in fig. 8. Panels (a1) and (b1) are for $(\alpha, \mu) = (0.5, -0.004861805)$ and $(\alpha, \mu) = (0.5, -0.0065)$, respectively.

and list in table 3. There is a Smale–horseshoe region **SH** after transitioning through $\mathbf{Q}_{\mathbf{0}}^{\Gamma_o}$; this region is discussed in more detail in section 6. Inside **SH**, the stable manifold $W^s(\mathbf{0})$ becomes tangent to the unstable manifold $W^u(\Gamma_o)$ of Γ_o at the bifurcation **F**, which plays the same role as the fold bifurcation curve of the heteroclinic orbit from **q** to **0** for cases **A** and **B** in [1, 12]. The other boundary of the Smale–horseshoe region **SH** is the codimension-one homoclinic bifurcation $\mathbf{Tan}_{\Gamma_o}$ of Γ_o, where $W^u(\Gamma_o)$ and $W^s(\Gamma_o)$ have a quadratic tangency. Past this bifurcation, there are no more homoclinic orbits of Γ_o and one finds small regions of existence of chaotic attractors [25], which are then destroyed via (reversed) period-doubling and saddle-node cascades of periodic orbits. This is discussed in more detail in section 7. The right-most period-doubling cascade in fig. 13, the one ending with $\mathbf{PD}_{\Gamma_t}$, changes Γ_t into an attracting periodic orbit Γ_t^a when ${}^2\Gamma_t^a$ disappears. The orbit Γ_t^a then disappears in the saddle-node bifurcation $\mathbf{SNP}_{\Gamma_o}$, where it merges with the only other remaining periodic orbit Γ_o; then, this marks the entry into region **2** is entered.

6 Smale–horseshoe region

Figure 14 shows the transition from the bifurcation $\mathbf{Q}_{\mathbf{0}}^{\Gamma_o}$ to the Smale–horseshoe region on the level of the intersection sets with the sphere $\mathbb{S}^*$. As before, the left column shows the numerically computed curves and the right column shows sketches where the gray and brown regions highlight the relative positions of the accumulation regions; each accumulation region is represented by the main intersection curve of the stable manifold of the saddle periodic orbit that exists on it. We present the stereographic projection at the codimension-one bifurcation $\mathbf{Q}_{\mathbf{0}}^{\Gamma_o}$ in panels (a1) and (a2). Notice in panel (a1) how one of the topological circles in $\widehat{W}^s(\Gamma_o)$ forms a connecting curve between the two intersection points in $\widehat{W}^{ss}(\mathbf{0})$, as a consequence of $W^s(\Gamma_o)$ accumulating on $W^{ss}(\mathbf{0})$ backward in time; see fig. 12. In this limiting case, all the accumulation regions accumulate onto this single curve $\widehat{W}^s(\Gamma_o)$, while spiraling around the other topological circle in $\widehat{W}^s(\Gamma_o)$. The boundary of $\widehat{\mathcal{B}}(\mathbf{q})$ is formed by $\widehat{W}^s(\Gamma_o)$ and the segment of $\widehat{W}^s(\mathbf{0})$ in beween the two points $\widehat{W}^{ss}(\mathbf{0})$. Before $\widehat{W}^s(\Gamma_o)$ connects the two points in $\widehat{W}^{ss}(\mathbf{0})$ at $\mathbf{Q}_{\mathbf{0}}^{\Gamma_o}$, infinitely many heteroclinic and homoclinic bifurcations must occur as the corresponding intersection sets accumulate in a spiraling manner onto $\widehat{W}^s(\Gamma_o)$; see panels (b1) and (b2) of fig. 11. This explain why the cascades of heteroclinic bifurcations $\mathbf{Q}_{\mathbf{0}}^{\Gamma_t}$ and homoclinic bifurcation accumulate onto the bifurcation curve $\mathbf{Q}_{\mathbf{0}}^{\Gamma_o}$ in fig. 5.

In panels (b1) and (b2) of fig. 14, after the heteroclinic bifurcation $\mathbf{Q}_{\mathbf{0}}^{\Gamma_o}$, the curve $\widehat{W}^s(\Gamma_o)$ that connected the two points $\widehat{W}^{ss}(\mathbf{0})$ now accumulates onto the topological circle in $\widehat{W}^s(\Gamma_o)$ that persists through this bifurcation. This accumulation is a consequence of the existence of the homoclinic orbits of Γ_o and the λ-lemma. Since there are infinitely many homoclinic orbits and heteroclinic cycles, there are infinitely many intersection curves in $\widehat{W}^s(\Gamma_o)$, $\widehat{W}^s(\Gamma_t)$, $\widehat{W}^s({}^2\Gamma_t)$, etc., that accumulate onto the topological circle in $\widehat{W}^s(\Gamma_o)$. Hence, the accumulation region in the intersection sets is more complicated; we illustrate this change by the brown shading in panel (b2). Note also that the boundary of the basin of attraction $\partial\widehat{\mathcal{B}}(\mathbf{q})$ of $\mathbf{q}$ after the bifurcation $\mathbf{Q}_{\mathbf{0}}^{\Gamma_o}$ in panels (b1) and (b2) has changed from two topological circles to a topological circle with two handles, that is, $\partial\widehat{\mathcal{B}}(\mathbf{q}) \subset \widehat{W}^s(\mathbf{0}) \cup \widehat{W}^s(\Gamma_o)$.

6.1 Dynamics inside the region SH

Past the codimension-one heteroclinic bifurcation $\mathbf{Q}_{\mathbf{0}}^{\Gamma_o}$ of system eq. (1), we find structurally stable homoclinic orbits of Γ_o; hence, there exist Smale–horseshoe dynamics in phase space [31]. Figure 15 (a) shows such homoclinic orbits (maroon and lilac curves) in more detail. The manifolds $W^s(\Gamma_o)$ (cyan surface) and $W^u(\Gamma_o)$ (orange surface) intersect along the homoclinic orbits Γ_o. Note how the outer boundary of the lower half of the topological cylinder $W^s(\Gamma_o)$ (black curve) accumulates in a spiraling fashion onto the top half of $W^s(\Gamma_o)$. Panel (b) shows an enlargement of panel (a) around the homoclinic orbits, where this accumulation is illustrated more clearly. The time series of the x-component of the two homoclinic orbits are shown in panels (c1) and (c2), and together in panel (c3). The lilac orbit moves faster away from Γ_o than the maroon orbit. The existence of these homoclinic orbits implies infinitely many secondary homoclinic orbits of Γ_o [31]. In addition, their existence also implies the appearance of heteroclinic cycles between different saddle periodic orbits, such as Γ_o, Γ_t, ${}^2\Gamma_t$, etc., due to the accumulation of their stable manifolds backward in time onto $W^s(\Gamma_o)$ and the accumulation of $W^u(\Gamma_o)$ onto their respective unstable manifolds.

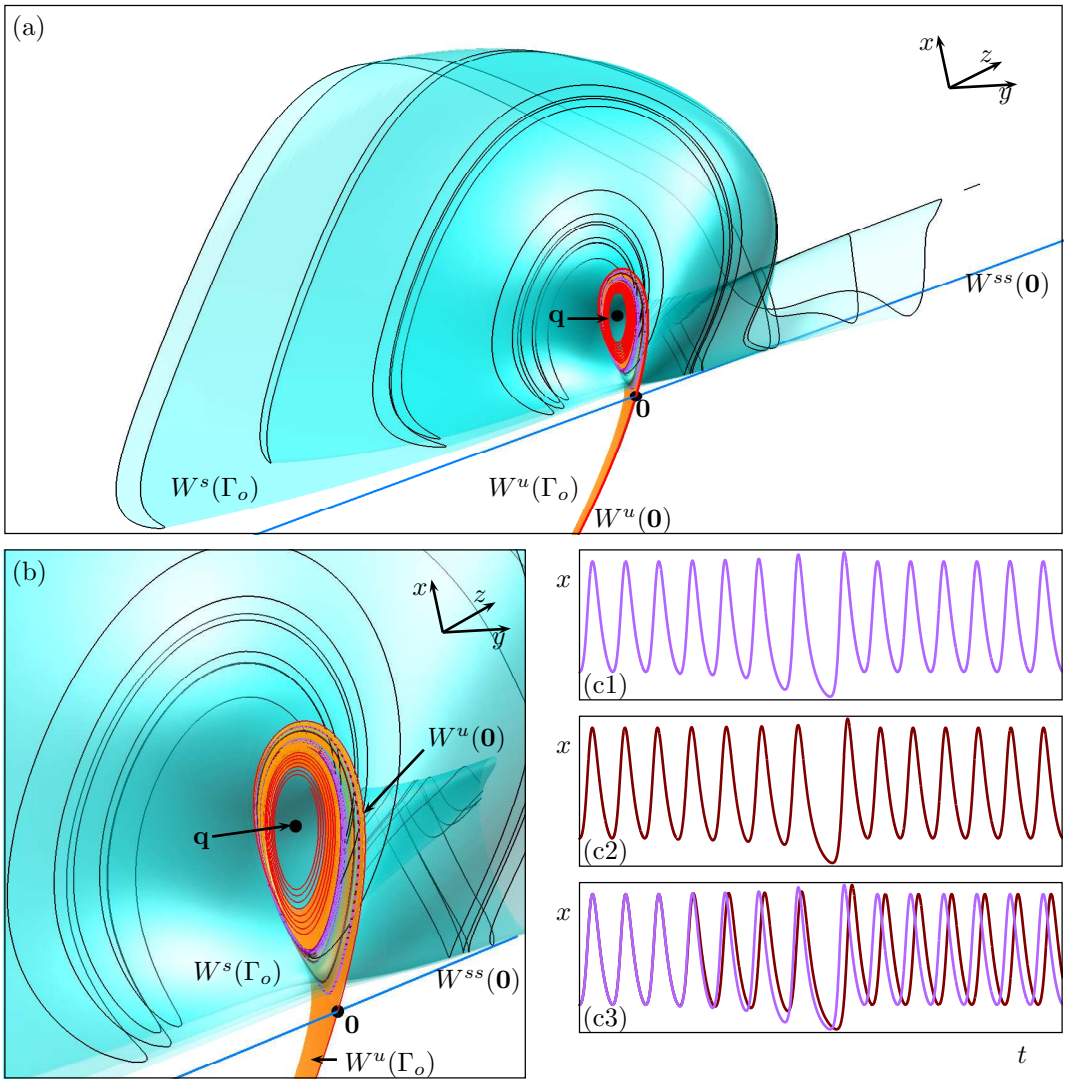

Figure 15: Configuration in phase space of $W^s(\Gamma_o)$ (cyan surface) and $W^u(\Gamma_o)$ (orange surface) of system eq. (1) in the Smale–horseshoe region. Panel (a) shows a big part of $W^s(\Gamma_o)$ and $W^u(\Gamma_o)$ in phase space; while panel (b) shows an enlargement of two transversal homoclinic orbits (maroon and lilac curves) of Γ_o. Panels (c1) and (c2) show the x-component of the transversal homoclinic orbits of Γ_o separately; while panel (c3) shows them together. Also shown are $W^u(\mathbf{0})$ (red curve) and $W^{ss}(\mathbf{0})$ (blue curve). The panels are for $(\alpha, \mu) = (0.5, -0.0065)$.

6.2 Transition through F

The numerical results shown in table 3 and fig. 5 indicate that the fold bifurcation **F**, in the vicinity of $\mathbf{C_I}$, occurs before the intersection between $W^u(\Gamma_o)$ and $W^s(\Gamma_o)$ becomes tangent, that is, before the bifurcation $\mathbf{Tan}_{\Gamma_o}$. The left column of fig. 16 illustrates the crossing of **F**, that is, the moment $W^u(\Gamma_o)$ (orange surface) is tangent to $W^s(\mathbf{0})$ (blue surface). Note the transversal intersection between $W^s(\mathbf{0})$ and $W^u(\Gamma_o)$ in panel (a1) that persists since its creation in region **1**. Since $\Gamma_o \to \Gamma_t \to \mathbf{0}$, there exist infinitely many heteroclinic orbits from Γ_o to $\mathbf{0}$, of which we only show two in panel (a1) (green curves). As **F** occurs, which is illustrated in panel (a2), the stable manifold $W^s(\mathbf{0})$ goes through a quadratic tangency with $W^u(\Gamma_o)$; this is similar to cases **A** and **B** [1, 12], where $W^s(\mathbf{0})$ exhibited a quadratic tangency with $W^u(\mathbf{q})$. In particular for case **C**, the infinitely many heteroclinic orbits merge in a tangent heteroclinic orbit, shown as the white curve in panel (a2). After the transition through **F** shown in panel (a3), $W^s(\mathbf{0})$ no longer intersects $W^u(\Gamma_o)$; hence, $W^s(\mathbf{0})$ no longer accumulates onto $W^s(\Gamma_o)$ and the unstable manifold $W^u(\mathbf{0})$ no longer bounds $W^u(\Gamma_o)$. In fact, we find that $W^s(\mathbf{0})$ no longer intersects any unstable manifold of any other saddle periodic orbit.

7 Transition to a strange attractor and period-doubling cascade

Past $\mathbf{Tan}_{\Gamma_o}$ one finds chaotic attractors, and cascades of period-doubling and saddle-node bifurcations. This allows system eq. (1) to transition back to region **2**; see section 4.

7.1 Transition through $\mathbf{Tan}_{\Gamma_o}$

The right column of fig. 16 illustrates the crossing of $\mathbf{Tan}_{\Gamma_o}$, that is, the last tangency between $W^u(\Gamma_o)$ (orange surface) and $W^s(\Gamma_o)$ (cyan surface). After the transition through **F** and before $\mathbf{Tan}_{\Gamma_o}$ occurs, the intersection between $W^s(\Gamma_o)$ and $W^u(\Gamma_o)$ still persists, as shown in panel (b1). As μ is decreased, system eq. (1) must exhibit a sequence of codimension-one homoclinic bifurcations of secondary tangencies between $W^s(\Gamma_o)$ and $W^u(\Gamma_o)$ [31], until it reaches the last homoclinic tangency at $\mathbf{Tan}_{\Gamma_o}$; shown in panel (b2). The bifurcation $\mathbf{Tan}_{\Gamma_o}$ represents the last intersection (blue curve) between $W^u(\Gamma_o)$ and $W^s(\Gamma_o)$. After the transition through $\mathbf{Tan}_{\Gamma_o}$, shown in panel (b3), the manifold $W^s(\Gamma_o)$ stops accumulating on itself, because it no longer intersects $W^u(\Gamma_o)$.

Figure 17 shows additional details of the transition through $\mathbf{Tan}_{\Gamma_o}$ by considering corresponding intersection sets with the sphere $\mathbb{S}^*$. Row (a) shows the situation in between the bifurcations **F** and $\mathbf{Tan}_{\Gamma_o}$ were the intersection set $\widehat{W}^s(\mathbf{0})$ is formed by a single closed curve; the left column shows the computed stereographic projections and the right column the corresponding sketches. Hence, the accumulation region (brown region) that is sketched in panel (a2) does not contain any intersection curves of $\widehat{W}^s(\mathbf{0})$. We find that the other intersection curves do not go through any significant changes for parameter values in between the bifurcations **F** and $\mathbf{Tan}_{\Gamma_o}$. Panels (b1) and (b2) illustrate the consequence of crossing $\mathbf{Tan}_{\Gamma_o}$. In particular, the intersection set $\widehat{W}^s(\Gamma_o)$ now consists of two single closed curves that do not accumulate onto any other intersection curve. Nevertheless, the existence of nontransversal intersections of the unstable manifolds of other saddle periodic orbits with $W^s(\Gamma_o)$ forces the other intersection curves to accumulate onto $\widehat{W}^s(\Gamma_o)$. Since there are no

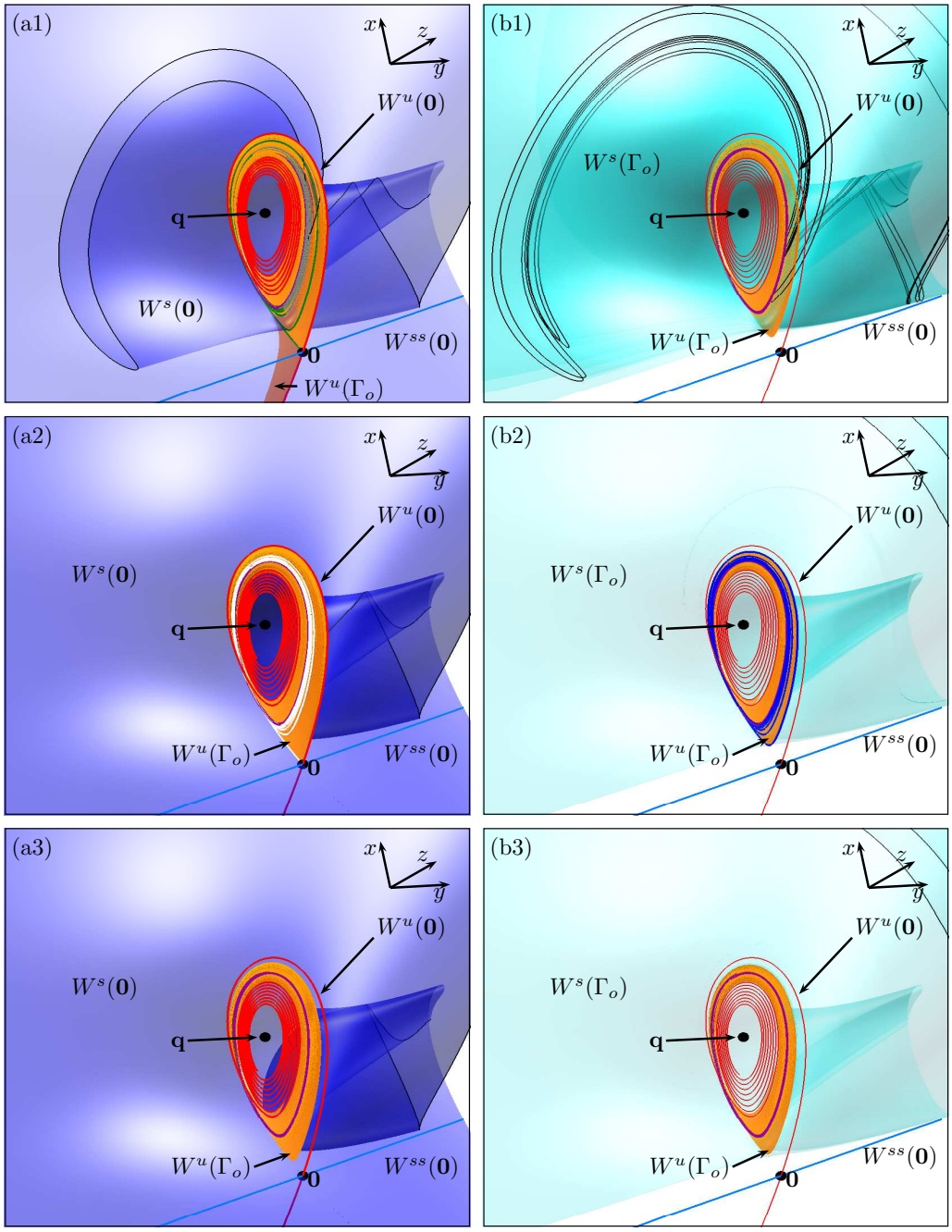

Figure 16: Phase portraits of the transition through the bifurcation curves **F** (left column) and $\mathbf{Tan}_{\Gamma_o}$ (right column) in system eq. (1). Shown are the effect of the transitions with respect to $W^s(\mathbf{0})$ and $W^u(\Gamma_o)$ (left column), and with respect to $W^s(\Gamma_o)$ and $W^u(\Gamma_o)$ (right column). Shown are $W^s(\mathbf{0})$ (blue surface), $W^s(\Gamma_o)$ (cyan surface) and $W^u(\Gamma_o)$ (orange surface); also shown are the corresponding tangency orbits (white and blue curves), $W^u(\mathbf{0})$ (red curve), and $W^{ss}(\mathbf{0})$ (blue curve). Panels (a1), (a2) and (a3) are for $(\alpha, \mu) = (0.5, -0.0065)$, $(\alpha, \mu) = (0.5, -0.007054355)$ and $(\alpha, \mu) = (0.5, -0.00706)$, respectively. Panels (b1), (b2) and (b3) are for $(\alpha, \mu) = (0.5, -0.00706)$, $(\alpha, \mu) = (0.5, -0.007076705)$ and $(\alpha, \mu) = (0.5, -0.0071)$, respectively.

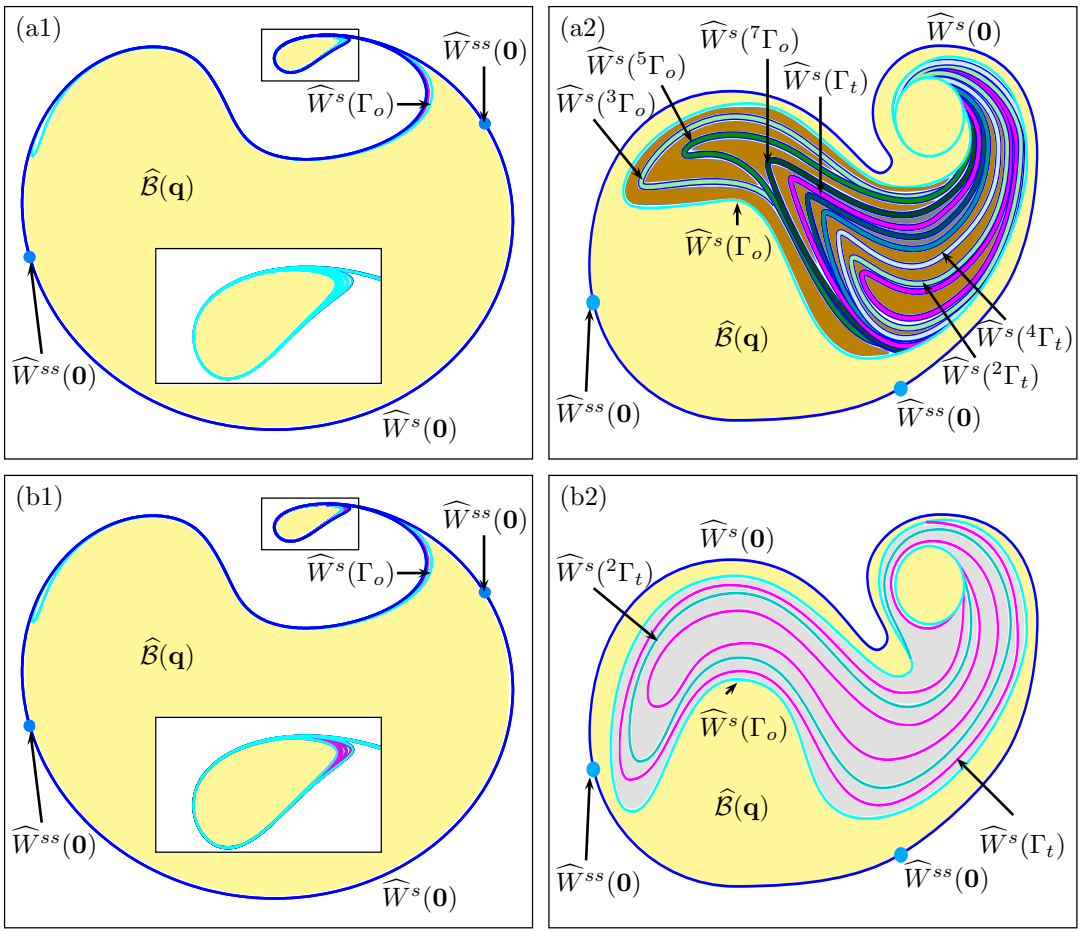

Figure 17: Stereographic projection of the intersection sets of the invariant manifolds with $\mathbb{S}^*$ after crossing the bifurcation curves $\mathbf{F}$ (top row) and $\mathbf{Tan}_{\Gamma_o}$ (bottom row). The left column shows the computed projections and the right column shows the corresponding sketches. The color code and labeling is the same as in fig. 8. Panels (a1) and (b1) are for $(\alpha, \mu) = (0.5, -0.00706)$ and $(\alpha, \mu) = (0.5, -0.0071)$, respectively.

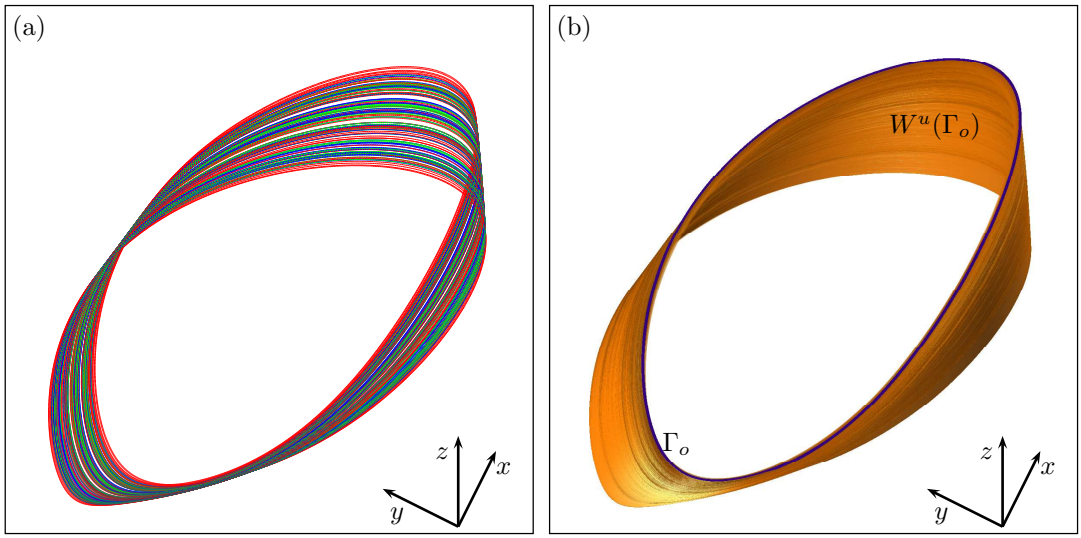

Figure 18: Approximation of the chaotic attractor of system eq. (1) close to the codimension-one homoclinic bifurcation $\mathbf{Tan}_{\Gamma_o}$ of Γ_o. Panel (a) shows three trajectories (red, blue and green), with initial conditions that differ in the sixth decimal place. Panel (b) shows a portion of $W^u(\Gamma_o)$. Here $(\alpha, \mu) \approx (0.5, -0.007076768)$.

homoclinic orbits of Γ_o anymore, we color the accumulation region light gray in panel (b2). As we will see in the next section, this region may correspond to the basin of attraction of a strange attractor or of an attracting periodic orbit. Note also that $\widehat{W}^s(\Gamma_o)$ is a topological annulus. The insets in panels (a1) and (b1) show enlargements around one of the topological circles of $W^s(\Gamma_o)$, illustrating the accumulation of $W^s(\Gamma_o)$ on itself and the lack of it before and after the transition through $\mathbf{Tan}_{\Gamma_o}$, respectively.

7.2 Evidence of the chaotic attractor

Figure 18 shows a chaotic attractor in the phase space of system eq. (1) for $\mu = -0.007076768$. Panel (a) shows trajectories of three different initial conditions that agree up to five decimal places. The trajectories are shown after their transients have been discarded, to illustrate that they are attracted to a lower-dimensional object in phase space. In particular, the trajectories do not remain arbitrarily close to each other as time progresses, but they do remain arbitrarily close to $W^u(\Gamma_t)$, which is shown in panel (b). This is evidence for the existence of a chaotic attractor, which would be the closure of $W^u(\Gamma_o)$.

As further evidence, fig. 19 shows the successive returns x_i^{Sc} to the plane $y = 0$ of the x-coordinates of each of these three trajectories, plotted as x_{i+1}^{Sc} versus x_i^{Sc}, where x_i^{Sc} is scaled to the interval $[0, 1]$. Clearly, the return map in fig. 19 is a unimodal map, which is effectively another clear indication that system eq. (1) has a chaotic attractor. In fact, it was proven that the Poincaré return map close to an inclination flip bifurcation of case **C**, up to some C^r-rescaling, is C^r-close to the family of unimodal maps $\psi_{\overline{a}}(u, v) = (0, 1 - \overline{a}v^2)$ [25]. We infer from figs. 18 and 19 that the closure of $W^u(\Gamma_o)$ can, therefore, be identified with the template of a type of Rössler attractor [11]. This implies that the strange attractor is destroyed by the tangency between $W^u(\Gamma_o)$ and $W^s(\Gamma_o)$, as was conjectured in [25]. Hence, $\mathbf{Tan}_{\Gamma_o}$ indeed separates the Smale–horseshoe region from the cascades of period-doubling and saddle-node bifurcations.

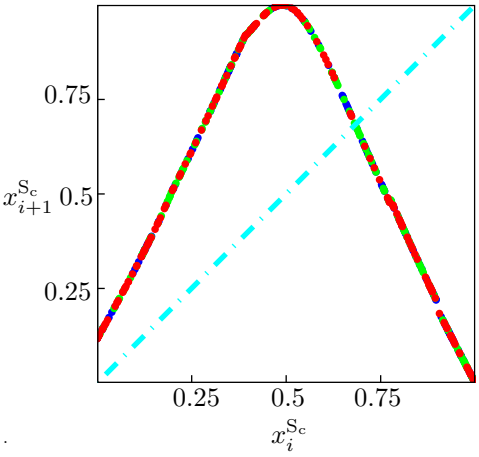

Figure 19: First return map of the scaled x-coordinates of the three trajectories shown in fig. 18 at the Poincaré section $y = 0$. The line $x_{i+1}^{S_c} = x_i^{S_c}$ is indicated (cyan dashed line) and the points are colored according to their corresponding trajectories in fig. 18.

7.3 Transition through PD back to region 2

The saddle periodic orbits that are created during the homoclinic and heteroclinic cascades disappear in cascades of period-doubling and saddle-node bifurcations as μ is decreased. During this process the intersection sets of different stable manifolds disappear with the corresponding periodic orbits. In fact, the accumulation region alternates between being a basin of attraction of an attracting periodic orbit and that of a strange attractor. This is caused by the saddle-node bifurcations that create periodic windows and start different period-doubling cascades [11]. These period-doubling and saddle-node cascades terminate at the final saddle-node bifurcation $\mathbf{SNP}_{\Gamma_o}$, which marks the transition back to region **2**.

Figure 20 illustrates the moment before and after the bifurcation $\mathbf{SNP}_{\Gamma_o}$ on the level of the intersection sets of invariant manifolds with $\mathbb{S}^*$; as before, the left column shows the computed stereographic projections and the right column the corresponding sketches. In panels (a1) and (a2), after the period-doubling bifurcation $\mathbf{PD}_{\Gamma_t}$, all periodic orbits have disappeared with the exception of Γ_o and an Γ_t, which is now attracting periodic orbit Γ_t^a. Immediately after the period-doubling bifurcation, Γ_t^a has a nonorientable strong stable manifold $W^{ss}(\Gamma_t^a)$; however, Γ_t^a becomes an attracting periodic orbit Γ_o^a with an orientable strong stable manifold before reaching $\mathbf{SNP}_{\Gamma_o}$. This transition from having a nonorientable and an orientable strong stable manifold occurs via a crossing of the curves $\mathbf{CC}^-_{\mathbf{\Gamma^a}}$ and $\mathbf{CC}^+_{\mathbf{\Gamma^a}}$ where the Floquet multipliers of Γ_t^a (Γ_o^a) change from being real positive (negative) to complex conjugate. In between these curves, the attracting periodic orbit Γ^a does not have a well-defined strong stable manifold [12]. We discuss the existence of the curves $\mathbf{CC}^{\pm}_{\Gamma^a}$ in more detail in section 8, when we study the unfolding over an even larger parameter range. On the level of the intersection sets shown in fig. 20(a), the former accumulation region has now become the basin of attraction $\widehat{\mathcal{B}}(\Gamma_t^a)$ of Γ_t^a (green). Furthermore, the basin $\widehat{\mathcal{B}}(\mathbf{q})$ is a disconnected region with boundaries $\widehat{W}^s(\Gamma_o)$ and $\widehat{W}^s(\mathbf{0})$. After, the saddle-node bifurcation $\mathbf{SNP}_{\Gamma_o}$, which marks the disappearance of Γ^a and Γ_o, we find ourselves again in region **2**, as is illustrated in panels (b1) and (b2). Hence, these panels are topological equivalent to panel **2** of fig. 8.

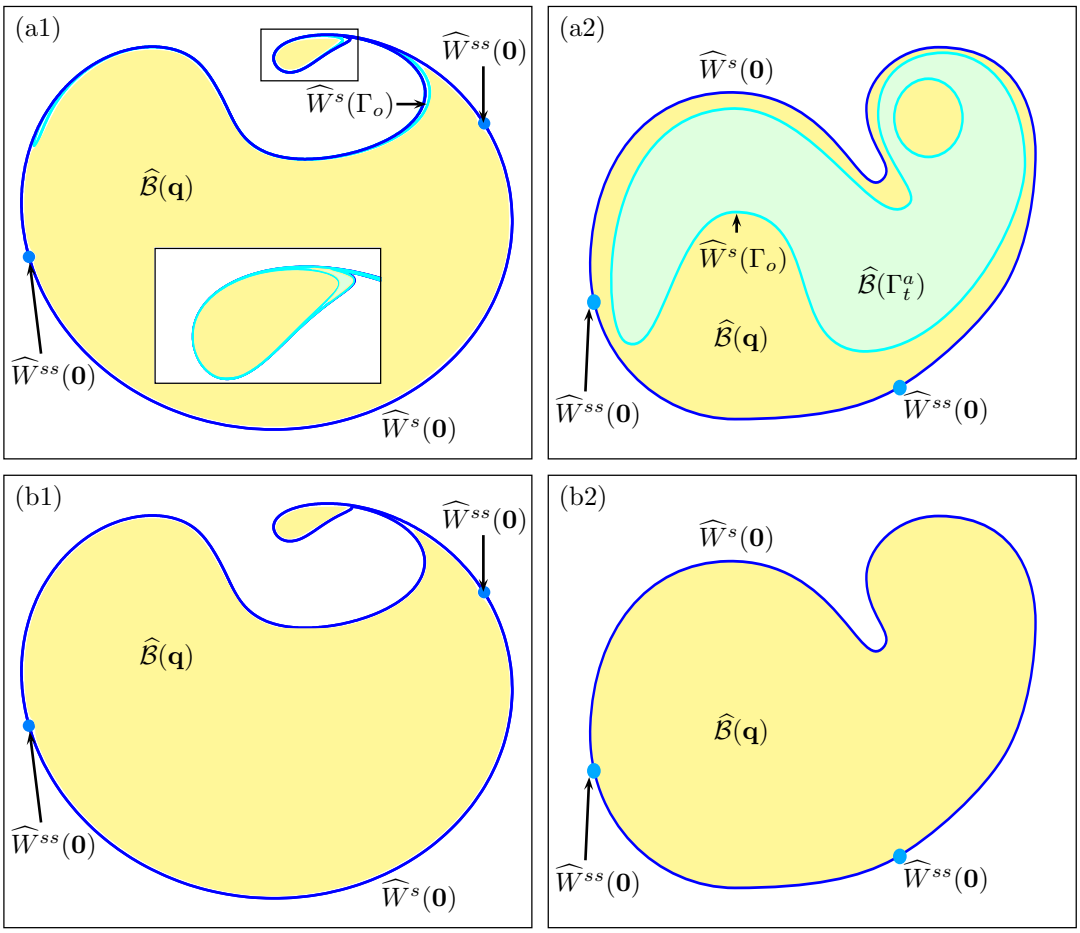

Figure 20: Stereographic projection of the intersection sets of the invariant manifolds with $\mathbb{S}^*$ before (top row) and after (bottom row) the last saddle-node bifurcation $\mathbf{SNP}_{\Gamma_o}$ of periodic orbits. The left column shows the computed projections and the right column shows the corresponding sketches. The color code and nomenclature of the regions is the same as given in fig. 8. Panels (a1) and (b1) are for $(\alpha, \mu) = (0.5, -0.0073)$ and $(\alpha, \mu) = (0.5, -0.0074)$, respectively.

8 Global picture in the (α, μ)-plane

We now focus our study on the global organization in the (α, μ)-parameter plane of the codimension-one bifurcations emanating from the homoclinic flip bifurcation point $\mathbf{C_I}$. Figure 21 shows the numerically computed bifurcation diagram of $\mathbf{C_I}$ for a much larger parameter range in panel (a), as well as two enlargements in panels (b) and (c). In particular, the parameter sweep of ζ now plays an even more prominent role in discerning small and subtle interactions of the different bifurcation curves. In fig. 21, we recognize from fig. 5 and table 3 the principal homoclinic branch (brown curve) with $\mathbf{C_I}$, as well as the curves of saddle-node bifurcation **SNP** (dark-green), of period-doubling bifurcation **PD** (red), of homoclinic bifurcation $\mathbf{Tan}_{\Gamma_o}$ (violet), of heteroclinic bifurcation $\mathbf{Q_0^{\Gamma_t}}$ (magenta), $\mathbf{Q_0^{\Gamma_o}}$ (purple) and $\mathbf{Q_0^{^2\Gamma_t}}[2\Gamma_o]$ (gray), and of homoclinic bifurcation $\mathbf{H_o}[m\Gamma_o, n\Gamma_t]$ $\mathbf{H_t}[m\Gamma_o, n\Gamma_t]$ (cyan curves). Note also the region **SH** where Smale–horseshoe dynamics occurs, and the curve **HB** of Hopf bifurcation (green curve) that transforms $\mathbf{q}$ into an unstable saddle focus. Panel (a) shows that the curve **HB** does not interact with any other bifurcation curve for μ-values larger than that at the generalized Hopf bifurcation point **GHB**. We also observe more clearly the curve $\mathbf{F}^*$ (dashed blue); recall that this curve represents the moment when $W^s(\mathbf{0})$ becomes tangent to $W^u(\mathbf{q})$, and it is the extension of the curve **F** past its intersection with $\mathbf{SNP}^*$, as shown in fig. 5. At first glance, $\mathbf{F}^*$ seems to bound the region where the homoclinic curves exists, but this is not the case, as we are going to discuss in more detail in the following section. We also show the curves $\mathbf{CC}^-_{\Gamma^a}$ and $\mathbf{CC}^+_{\Gamma^a}$ (orange) which represent the moment the Floquet multipliers of the attracting periodic orbit Γ^a become complex conjugate with negative and positive real parts, respectively. In addition, we also present the curve $\mathbf{CC}^-_{^2\Gamma^a}$ (dark orange) of the attracting periodic orbit $^2\Gamma^a$; these are visible in panels (b) and (c).

The curves $\mathbf{Q_0^{\Gamma_t}}$ shown in fig. 21 extend to the top part of the figure in panel (a). They represent the extensions of the heteroclinic bifurcation curves in fig. 5 past the transition of Γ_t to the attracting periodic orbit Γ^a_t, where $\mathbf{Q_0^{\Gamma_t}}$ corresponds to the intersection of the two-dimensional strong stable manifold $W^{ss}(\Gamma^a_t)$ with $W^u(\mathbf{0})$, which is also a codimension-one phenomenon. As such, these curves terminate at the respective curve $\mathbf{CC}^-_{\Gamma^a}$, that is, at the moment when $W^{ss}(\Gamma^a_t)$ is no longer well defined. This also holds for the heteroclinic bifurcation $\mathbf{Q_0^{^2\Gamma_t}}[2\Gamma_o]$ (gray curve), which can be seen to terminate at $\mathbf{CC}^-_{^2\Gamma^a}$ in fig. 21(b).

8.1 Cascades of inclination flip bifurcations

The larger parameter range in fig. 21(a) reveals how the homoclinic bifurcations, which were hard to discern in fig. 5, fan out and are more distinguishable. Furthermore, we clearly see how each homoclinic bifurcation curve encloses a region in the (α, μ)-plane with a constant ζ value; indeed, the ζ-value in each region increases as a heteroclinic bifurcation $\mathbf{Q_0^{\Gamma_t}}$ or $\mathbf{Q_0^{^2\Gamma_t}}$ is approached; see also section 5.

It is an important feature of fig. 21 that many of the homoclinic, saddle-node and period-doubling bifurcation curves emanating from $\mathbf{C_I}$ end at other codimension-two inclination flip bifurcation points. Notably, the principal homoclinic branch goes through a secondary inclination flip bifurcation $\mathbf{B^*_I}$ of case **B**, which is the end point of the curves $\mathbf{^2H_o}$ and $\mathbf{PD}_{\Gamma_t}$. Moreover, other homoclinic curves exhibit inclination flip bifurcations $\mathbf{C^n_I}$ of case **C**, where n represents the number of loops that the corresponding homoclinic orbit makes in phase space.

The bifurcation diagram near one of these inclination flip points, $\mathbf{C^3_I}$, is shown in fig. 21(b). Notice how $\mathbf{C^3_I}$ is responsible for the transformation of the orientable homoclinic bifurcation

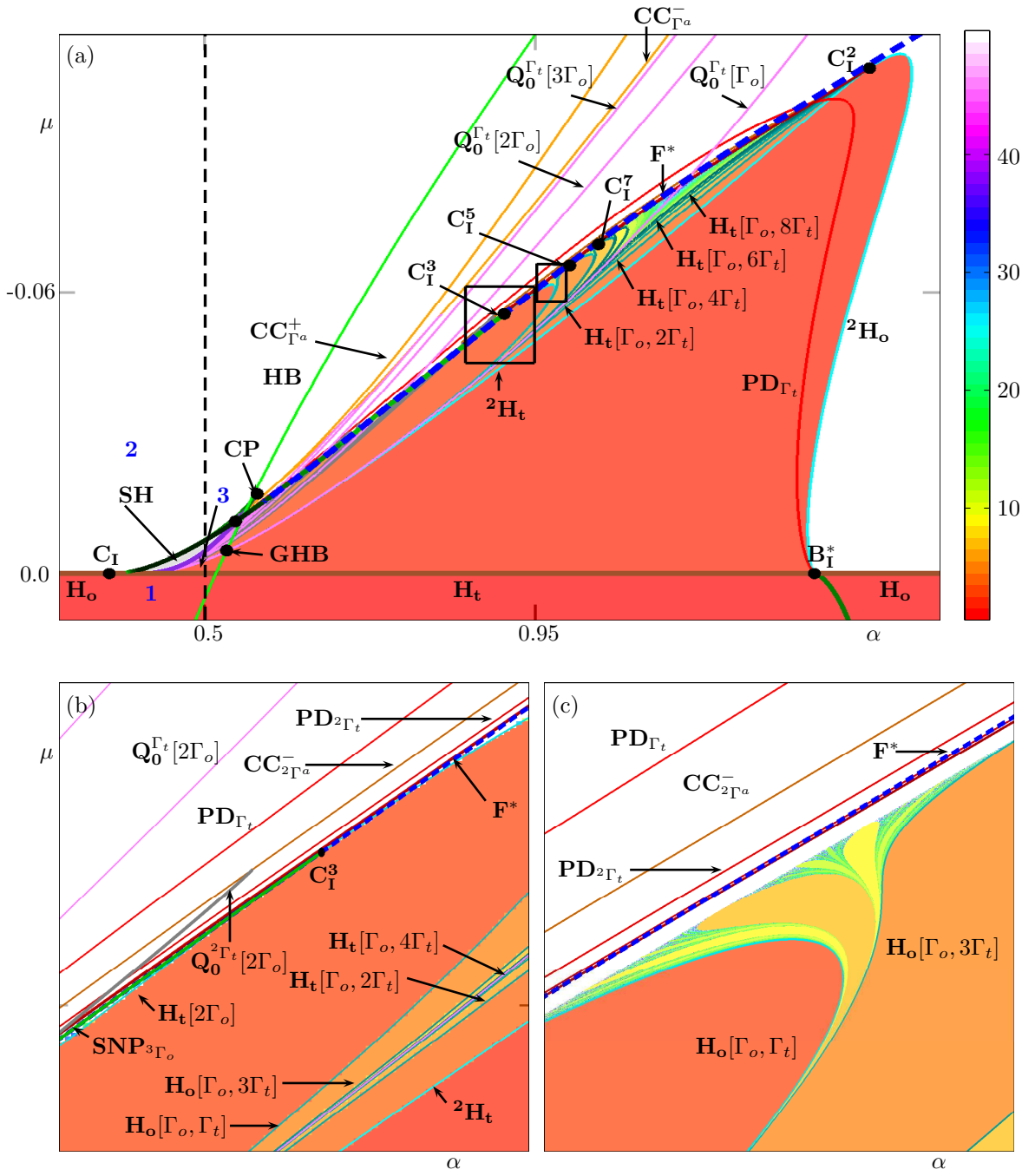

Figure 21: Bifurcation diagram of system eq. (1) for a larger region in the (α, μ)-plane than shown in fig. 5. Panels (b) and (c) are enlargements as indicated in panel (a). The color code of the regions and labeling of the curves are the same as in fig. 5. We also show the curve $\mathbf{Q}_\mathbf{0}^{^2\Gamma_t}$ (gray), and the curves $\mathbf{CC}^{\pm}_{\Gamma^a}$ and $\mathbf{CC}^{-}_{^2\Gamma^a}$ (orange) of Γ^a and $^2\Gamma^a$, respectively.

$\mathbf{H_o}[\Gamma_o, \Gamma_t]$ to the nonorientable homoclinic bifurcation $\mathbf{H_t}[2\Gamma_o]$, both of which emanate from the initial inclination flip bifurcation $\mathbf{C_I}$. Recall that these homoclinic bifurcations are related as they represent the last and the first bifurcation of their respective accumulation cluster, as discussed in section 5.4. Moreover, they create the saddle periodic orbits ${}^3\Gamma_o$ and ${}^3\Gamma_t$, respectively, and they bound a region in the parameter plane where $\zeta = 3$; see also fig. 13. So it does not come as a surprise that $\mathbf{SNP}_{{}^3\Gamma_o}$ (green curve) ends at the bifurcation point $\mathbf{C_I^3}$, as this bifurcation curve is responsible for the disappearance of ${}^3\Gamma_o$ and ${}^3\Gamma_t$; indeed $\mathbf{SNP}_{{}^3\Gamma_o}$ plays the same role as $\mathbf{SNP}_{\Gamma_o}$ in the unfolding of $\mathbf{C_I}$. In Figure 21(c) we observe that $\mathbf{H_o}[\Gamma_o, \Gamma_t]$ turns around before reaching $\mathbf{C_I^3}$, and then the curve continues smoothly past $\mathbf{C_I^3}$ as $\mathbf{H_t}[2\Gamma_o]$ before returning to $\mathbf{C_I}$. This same scenario can also be observed for the inclination flip points $\mathbf{C_I^5}$ and $\mathbf{C_I^7}$. Moreover, fig. 21(c) shows that there exist infinitely many regions with constant ζ in between the two inclination flip points $\mathbf{C_I^3}$ and $\mathbf{C_I^5}$. The boundaries of each of these regions are homoclinic bifurcation curves emanating from $\mathbf{C_I}$, which also exhibit an inclination flip bifurcation of case $\mathbf{C}$ along them and then come back to $\mathbf{C_I}$ as an homoclinic bifurcation curve of the opposite orientation. As a consequence, the respective saddle-node and period-doubling bifurcation curves extend from $\mathbf{C_I}$ to this additional inclination flip bifurcation point.

8.2 Homoclinic bubbles

This type of overall bifurcation structure generated by a particular homoclinic curve is called a homoclinic bubble [16]. Recall our discussion of the gaps between accumulation clusters along the slice $\mu = 0.5$, which we found in table 3 and sketched in fig. 13. Figure 21 (a) shows that the pairs of homoclinic bifurcations $\mathbf{H_o}[m\Gamma_o, \Gamma_t]$ and $\mathbf{H_t}[(m+1)\Gamma_o]$, as found for $m = 1, 2, 3, 4, 5, 6, 7, 8, 9$ in table 3 form bubbles in the parameter plane. In particular, identified cascades of these bubbles explain the disappearance of the infinitely many codimension-one curves that emanate from the unfolding of case $\mathbf{C}$ during a transition to case $\mathbf{B}$. In fact, two types of bubbles were conjectured [16] and subsequently confirmed numerically [27]: one is characterized by a homoclinic-doubling cascade and the other by an additional homoclinic flip bifurcation of case $\mathbf{C}$. Figure 22 (a) shows the theoretical sketch of a single homoclinic k-bubble, for $k \in \mathbb{N}$, of the latter type, reproduced from [16]. Notice how an orientable k-homoclinic bifurcation curve H_o^k emanates from the principal homoclinic flip bifurcation point $\mathbf{C_{out}}$ and then exhibits an inclination flip bifurcation $\mathbf{C_{out}^k}$, after which it is the nonorientable k-homoclinic bifurcation curve H_t^k. In this way, the homoclinic and period-doubling bifurcation curves of the form $2^n k$, for $n \in \mathbb{N}$, emanating from $\mathbf{C_{out}}$ disappear in the unfolding of $\mathbf{C_{out}^k}$. For any $k \in \mathbb{N}$, there exists k-bubbles that annihilate all the corresponding $2^n k$ curves of $\mathbf{C_{out}}$. Those are exactly the bifurcation structures we observe in the bifurcation diagram of fig. 21 in the transition between the inclination flip points $\mathbf{C_I}$ and $\mathbf{B_I^*}$.

Figure 22(b) shows a different enlargement of the bifurcation diagram of $\mathbf{C_I}$. Here, we use the coordinate transformation $\mu^* := \mu + 0.1246\alpha - 0.06644$ and plot the bifurcation diagram in the (α, μ^*)-plane to improve visualization and comparison with the sketch in panel (a). The homoclinic curve $\mathbf{{}^2H_t}$ exhibits the inclination flip bifurcation $\mathbf{C_I^2}$, which allows $\mathbf{{}^2H_t}$ to become $\mathbf{{}^2H_o}$ so it can disappear at $\mathbf{B_I^*}$. This is one of the most important curves in the transition between the two cases [16]. However, it does not form a bubble as presented in [16] because both homoclinic curves do not emanate from the same point $\mathbf{C_I}$. Nevertheless, the inclination flip point $\mathbf{C_I^2}$ plays the same role as the homoclinic flip point $\mathbf{C_{out}^k}$ of a k-bubble for $k = 2$ in terms of absorbing/generating the respective bifurcation curves. Notice in fig. 21(b) how the cascade of nonorientable homoclinic bifurcation curves (cyan) of the

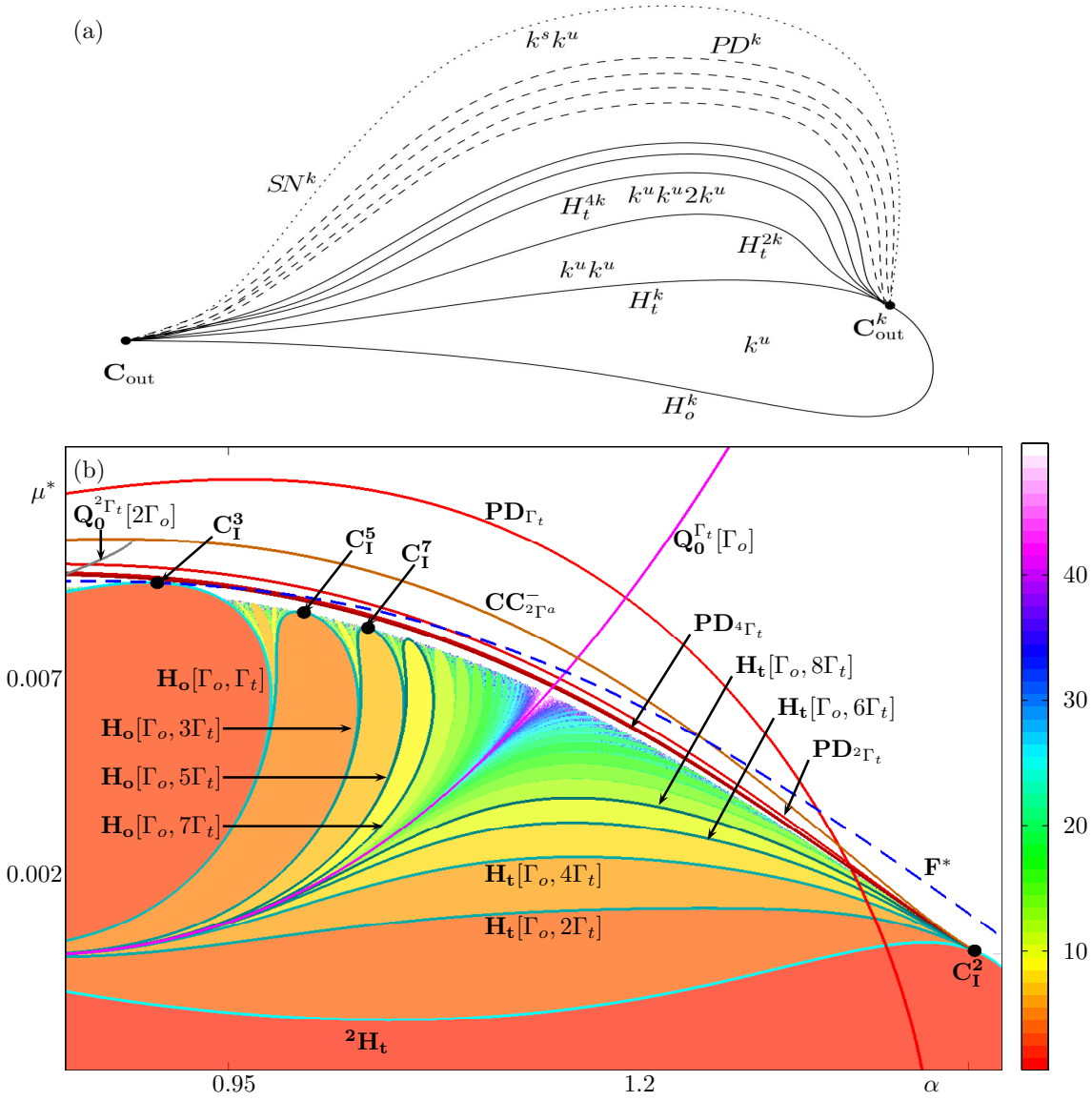

Figure 22: Comparison of a theoretical and numerical inclination flip bubble. Panel (a) shows the sketch of an inclination flip bubble from [16, Fig. 12]; panel (b) shows a region of fig. 21 in the (α, μ^*)-plane, where $\mu^* := \mu + 0.1246\alpha - 0.06644$. Color code of the regions and nomenclature of the curves are as in fig. 21. [The inset is reproduced from Journal of Dynamics and Differential Equations, Resonant Homoclinic Flip Bifurcations, 12(4), 2000, pages 807-850, A. J. Homburg and B. Krauskopf, ©Plenum Publishing Corporation 2000 with permission of Springer.]

form $\mathbf{H_t}[\Gamma_o, n\Gamma_t]$, for $n = 2, 4, 6, 8$, and the period-doubling bifurcation curves $\mathbf{PD}_{2\Gamma_t}$ and $\mathbf{PD}_{4\Gamma_t}$ (red) connect the points $\mathbf{C_I}$ and $\mathbf{C_I^2}$ as sketched in panel (a).

The same phenomenon occurs at the points $\mathbf{C_I^3}$, $\mathbf{C_I^5}$, and $\mathbf{C_I^7}$, but the curves are much closer together. Figure 22(b) clearly shows the complicated structure of how some homoclinic bifurcation curves create bubbles and others connect to inclination flip points on bubbles. It also shows how infinitely many homoclinic bubbles accumulate on $\mathbf{Q_0^{\Gamma_t}}[\Gamma_o]$, which is illustrated by the increase of ζ. Furthermore, notice how the ζ-value also increases in the different regions in between bubbles, such as those of $\mathbf{C_I^3}$, $\mathbf{C_I^5}$ and $\mathbf{C_I^7}$, each of which is associated with a codimension-one heteroclinic bifurcation of the type $\mathbf{Q_0^{\Gamma^*}}$ for a suitable saddle periodic orbit Γ^*; see section 5. The accumulation of these homoclinic bifurcation curves and bubbles onto a heteroclinic bifurcation of the form $\mathbf{Q_0^{\Gamma_t}}$ was not identified in either in [16] or [27]. Another interesting detail about the bubbles in Figure 21(b) is how they seem to be bounded by a single smooth curve, where the inclination flip points $\mathbf{C_I^3}$, $\mathbf{C_I^5}$ and $\mathbf{C_I^7}$ occur along it. At first glance, it appears that this curve is $\mathbf{F}^*$, that is, the fold curve of a tangency between $W^u(\mathbf{q})$ and $W^s(\mathbf{0})$, as shown in panel (a) and (b) in fig. 21. However, fig. 22 (b) indicates that this is not the case. This boundary curve represents a boundary crisis [29], and infinitely many inclination flip bifurcations of case $\mathbf{C}$ occur along it. We believe that this curve of boundary crisis involves the tangency of an, as yet, unknown invariant object.

Finally, we remark that the eigenvalues of $\mathbf{0}$ do not change as α and μ vary in the bifurcation diagrams shown in fig. 21 and fig. 22; see section 2.1. This raises the question of the existence of $\mathbf{B_I^*}$ in fig. 21, because it fullfils the eigenvalue conditions of case $\mathbf{C}$. Preliminary work suggest that it also fullfils the necessary geometry condition for case $\mathbf{C}$. On the other hand, our bifurcation analysis clearly identifies the point $\mathbf{B_I^*}$ as an inclination flip bifurcation of case $\mathbf{B}$. Further analysis of this codimension-two point is beyond the scope of this paper, and left for future work.

9 Discussion

We presented a detailed study of the unfolding of a codimension-two inclination flip bifurcation of case $\mathbf{C}$ by computing the representative manifolds of saddle objects in system eq. (1) as well as their bifurcation curves in the (α, μ)-plane. In the same spirit as in [1, 12], we chose representative points in regions with distinct qualitative behavior, and illustrated the changes and consequences when different bifurcation curves are crossed. To this end, we presented the global invariant manifolds in phase space as well as their intersection sets with a suitable sphere. Clearly, case $\mathbf{C}$ is much more complicated than cases $\mathbf{A}$ and $\mathbf{B}$. Indeed, one can find Smale–horseshoe dynamics, strange attractors and cascades of homoclinic, period-doubling and saddle-node bifurcations in the neighborhood of this codimension-two point in the (α, μ)-plane. Representative homoclinic, heteroclinic, saddle-node and period-doubling bifurcations were computed in the (α, μ)-parameter plane and they agree with and extend the theoretical unfolding described in [15].

In pursuit of a better understanding of this unfolding, we defined a winding number ζ and performed a parameter sweep in the (α, μ)-plane to delimit regions with different ζ-values. We found that certain boundaries of these regions correspond to homoclinic bifurcations that emanate from the inclination flip point but had not been identified before. We also found that the homoclinic bifurcations reorganize themselves in different cascades that accumulate onto codimension-one heteroclinic bifurcations that involve different saddle periodic orbits, e.g. the nonorientable saddle periodic orbit Γ_t, and the equilibrium $\mathbf{0}$ [21]. These homoclinic and heteroclinic cascades can be distinguished in phase space according to the number of

rotations that the respective homoclinic or heteroclinic orbit makes around different saddle periodic orbits. We computed and represented the overall implications of these bifurcations near $\mathbf{C_I}$. We also identified the boundaries of the Smale–horseshoe region as the codimension-one heteroclinic bifurcation $\mathbf{Q_0^{\Gamma_o}}$, where there is a connecting orbit from $\mathbf{0}$ to the orientable saddle periodic orbit Γ_o. The other boundary is the codimension-one homoclinic bifurcation $\mathbf{Tan}_{\Gamma_o}$ of Γ_o. The bifurcation $\mathbf{Tan}_{\Gamma_o}$ was conjectured to exist [25]; it is tied to the destruction of a strange attractor, because it marks the termination of the period-doubling cascade. The bifurcation curves $\mathbf{Q_0^{\Gamma_o}}$ and $\mathbf{Tan}_{\Gamma_o}$ intersect to form a codimension-two heteroclinic cycle between $\mathbf{0}$ and the orientable saddle periodic orbit Γ_o, thus, delimiting a bounded connected region in the (α, μ)-plane where system eq. (1) exhibits Smale–horseshoe dynamics.

We also studied the global bifurcation picture in the (μ, α)-plane to determine the overall organization of the codimension-one bifurcations emanating from the homoclinic flip point of case **C**. We found a complex picture involving the transition to an inclination flip bifurcation of case **B**. We found that the certain homoclinic bifurcations create bubbles in parameter plane, which exhibit an additional homoclinic flip bifurcation of case **C** that changes the orientation of the respective homoclinic bifurcation. These bubbles were proposed as a crucial ingredient in the transition between cases **B** and **C** as codimension-three phenomena [16], and found numerically in [27]. We studied in unprecedented detail the role of the heteroclinic bifurcations in the existence of these infinitely many bubbles and described their accumulation on a specific boundary curve.

Overall, the work presented here shows a detailed numerical and theoretical exploration of the most complicated case of a homoclinic flip bifurcation. The results obtained illustrate different phenomena that were not considered before for case **C** and could, in principle, be extended to a more abstract and general setting. In particular, this paper exemplifies the important role numerical studies can play, not just in applications, but also for a better understanding of theoretical constructs. A deeper insight into phenomena can be obtained that had not yet been considered due to the intricacies of the theory. In fact, theoretical constructions that might seem esoteric at first glance and devoid of direct use, can be put into a concrete context thanks to their detection with advanced numerical techniques. Beyond a contributions to the theory, most of our results may be of interest to applications that exhibit homoclinic flip bifurcations. For example, it has been found that a combination of homoclinic flip bifurcation and fast-slow dynamics can explain the creation of large spiking excursions of periodic orbits, for example in the Hindmarsh–Rose model [23].

A lot of interesting questions arise from our study of homoclinic flip bifurcations, which we would like to address in the future. One of them concerns the configuration of manifolds responsible for the inward twist case $\mathbf{C_{in}}$. It is clear from the theory that the relative position of the Smale–horseshoe region in the parameter plane is different. For this reason, the boundaries of this region might differ from the ones found here. However, we have no concrete example of a three-dimensional vector field exhibiting this particular flavor of case **C** and, as such, are not yet in a position to explore this particular case. We are also interested in understanding the geometric conditions that give rise to the homoclinic flip point $\mathbf{B_I^*}$ of case **B** in the bifurcation diagram of case **C** in fig. 21.

More generally, the results presented here can be seen as a showcase of the capabilities of advanced numerical methods based on two-point boundary value problems for the bifurcation analysis of a given system with complicated global bifurcations. Since global bifurcations have attracted considerable attention recently as organizing centers for spiking, pulsing and bursting, we hope that the work in this paper may contribute to future insights into theory and applications alike.

References

[1] P. Aguirre, B. Krauskopf, and H. M. Osinga, *Global invariant manifolds near homoclinic orbits to a real saddle: (Non)orientability and flip bifurcation*, SIAM J. Appl. Dyn. Syst., 12 (2013), pp. 1803–1846.

[2] R. Barrio, M. Lefranc, M. A. Martínez, and S. Serrano, *Symbolic dynamical unfolding of spike-adding bifurcations in chaotic neuron models*, EPL (Europhysics Letters), 109 (2015).

[3] R. Barrio and A. Shilnikov, *Parameter-sweeping techniques for temporal dynamics of neuronal systems: case study of hindmarsh-rose model*, J. Math. Neurosci., 1 (2011).

[4] R. Barrio, A. Shilnikov, and L. Shilnikov, *Kneadings, symbolic dynamics and painting Lorenz chaos*, Internat. J. Bifur. Chaos Appl. Sci. Engrg., 22 (2012).

[5] R. C. Calleja, E. J. Doedel, A. R. Humphries, A. Lemus-Rodriguez, and E. B. Oldeman, *Boundary-value problem formulations for computing invariant manifolds and connecting orbits in the circular restricted three body problem*, Celest. Mech. Dyn. Astron., 114 (2012), pp. 77–106.

[6] A. R. Champneys, V. Kirk, E. Knobloch, B. E. Oldeman, and J. D. M. Rademacher, *Unfolding a tangent equilibrium-to-periodic heteroclinic cycle*, SIAM J. Appl. Dyn. Syst., 8 (2009), pp. 1261–1304.

[7] A. R. Champneys, Y. Kuznetsov, and B. Sandstede, *A numerical toolbox for homoclinic bifurcation analysis*, Internat. J. Bifur. Chaos Appl. Sci. Engrg., 6 (1996), pp. 867–887.

[8] B. Deng, *Homoclinic twisting bifurcations and cusp horseshoe maps*, J. Dynam. Differential Equations, 5 (1993), pp. 417–467.

[9] E. J. Doedel, *AUTO: A program for the automatic bifurcation analysis of autonomous systems*, Congr. Numer., 30 (1981), pp. 265–284.

[10] E. J. Doedel and B. E. Oldeman, *AUTO-07p: Continuation and Bifurcation Software for Ordinary Differential Equations*, Department of Computer Science, Concordia University, Montreal, Canada, 2010. With major contributions from A. R. Champneys, F. Dercole, T. F. Fairgrieve, Y. Kuznetsov, R. C. Paffenroth, B. Sandstede, X. J. Wang and C. H. Zhang; available at http://www.cmvl.cs.concordia.ca/.

[11] R. Gilmore and M. Lefranc, *The Topology of Chaos: Alice in Stretch and Squeezeland*, Wiley-Interscience, 2002.

[12] A. Giraldo, B. Krauskopf, and H. M. Osinga, *Saddle invariant objects and their global manifolds in a neighborhood of a homoclinic flip bifurcation of case B*, SIAM J. Appl. Dyn. Syst., 16 (2017), pp. 640–686.

[13] A. Golmakani and A. J. Homburg, *Lorenz attractors in unfoldings of homoclinic-flip bifurcations*, Dyn. Syst., 26 (2011), pp. 61–76.

[14] J. Guckenheimer and P. Holmes, *Nonlinear Oscillations, Dynamical Systems, and Bifurcations of Vector Fields*, Springer-Verlag, New York, 1983.

[15] A. J. Homburg, H. Kokubu, and M. Krupa, *The cusp horseshoe and its bifurcations in the unfolding of an inclination-flip homoclinic orbit*, Ergodic Theory Dynam. Systems, 14 (1994), pp. 667–693.

[16] A. J. Homburg and B. Krauskopf, *Resonant homoclinic flip bifurcations*, J. Dynam. Differential Equations, 12 (2000), pp. 807–850.

[17] A. J. Homburg and B. Sandstede, *Homoclinic and heteroclinic bifurcations in vector fields*, in Handbook of Dynamical Systems, H. W. Broer, B. Hasselblatt, and F. Takens, eds., vol. 3, Elsevier, New York, 2010, pp. 381–509.

[18] M. Kisaka, H. Kokubu, and H. Oka, *Bifurcations to n-homoclinic orbits and n-periodic orbits in vector fields*, J. Dynam. Differential Equations, 5 (1993), pp. 305–357.

[19] M. Koper, *Bifurcations of mixed-mode oscillations in a three-variable autonomous Van der Pol-Duffing model with a cross-shaped phase diagram*, Phys. D, 80 (1995), pp. 72–94.

[20] B. Krauskopf and H. M. Osinga, *Computing invariant manifolds via the continuation of orbit segments*, in Numerical Continuation Methods for Dynamical Systems: Path Following and Boundary Value Problems, B. Krauskopf, H. M. Osinga, and J. Galán-Vioque, eds., Springer, The Netherlands, 2007, pp. 117–154.

[21] B. Krauskopf and T. Riess, *A Lin's method approach to finding and continuing heteroclinic connections involving periodic orbits*, Nonlinearity, 21 (2008), pp. 1655–1690.

[22] Y. A. Kuznetsov, O. Feo, and S. Rinaldi, *Belyakov homoclinic bifurcations in a tritrophic food chain model*, SIAM J. Appl. Dyn. Syst., 62 (2001), p. 462487.

[23] D. Linaro, A. Champneys, M. Desroches, and M. Storace, *Codimension-two homoclinic bifurcations underlying spike adding in the Hindmarsh-Rose burster*, SIAM J. Appl. Dyn. Syst., 11 (2012), pp. 939–962.

[24] A. Lohse and A. Rodrigues, *Boundary crisis for degenerate singular cycles*, Nonlinearity, 30 (2017), pp. 2211–2245.

[25] V. Naudot, *Strange attractor in the unfolding of an inclination-flip homoclinic orbit*, Ergodic Theory Dynam. Systems, 16 (1996), pp. 1071–1086.

[26] V. Naudot, *A strange attractor in the unfolding of an orbit-flip homoclinic orbit*, Dyn. Syst., 17 (2002), pp. 45–63.

[27] B. E. Oldeman, B. Krauskopf, and A. R. Champneys, *Numerical unfoldings of codimension-three resonant homoclinic flip bifurcations*, Nonlinearity, 14 (2001), pp. 597–621.

[28] H. M. Osinga, *Nonorientable manifolds in three-dimensional vector fields*, Internat. J. Bifur. Chaos Appl. Sci. Engrg., 13 (2003), pp. 553–570.

[29] H. M. Osinga, *Locus of boundary crisis: Expect infinitely many gaps*, Phys. Rev. E, 74 (2006).

[30] J. Palis and W. de Melo, *Geometric Theory of Dynamical Systems*, Springer, New York, 1982.

[31] J. Palis and F. Takens, *Hyperbolicity and Sensitive Chaotic Dynamics at Homoclinic Bifurcations: Fractal Dimensions and Infinitely Many Attractors in Dynamics*, Cambridge University Press, 1995.

[32] B. Sandstede, *Verzweigungstheorie Homokliner Verdopplugen*, PhD thesis, University of Stuttgart, Stuttgart, Germany, 1993.

[33] B. Sandstede, *Constructing dynamical systems having homoclinic bifurcation points of codimension two*, J. Dynam. Differential Equations, 9 (1997), pp. 269–288.

[34] L. P. Shilnikov, *A case of the existence of a denumerable set of periodic motions*, Sov. Math. Dokl., 6 (1965), pp. 163–166.

[35] L. P. Shilnikov, *On the generation of a periodic motion from trajectories doubly asymptotic to an equilibrium state of saddle type*, Mat. Sb. (N.S.), 77(119) (1968), pp. 461–472.

[36] L. P. Shilnikov, A. L. Shilnikov, D. V. Turaev, and L. O. Chua, *Methods of Qualitative Theory in Nonlinear Dynamics (Part* I*)*, vol. 4, World Scientific, Singapore, 1998.

[37] B. W., A. Champneys, E. Doedel, W. Govaerts, Y. Kuznetsov, and B. Sandstede, *Numerical continuation, and computation of normal forms*, in Handbook of Dynamical Systems, 1999.

[38] S. M. Wieczorek, *Global bifurcation analysis in laser systems*, in Numerical Continuation Methods for Dynamical Systems: Path Following and Boundary Value Problems, B. Krauskopf, H. M. Osinga, and J. Galán-Vioque, eds., Springer, The Netherlands, 2007, pp. 177–220.

[39] S. M. Wieczorek and B. Krauskopf, *Bifurcations of n-homoclinic orbits in optically injected lasers*, Nonlinearity, 18 (2005), pp. 1095–1120.

[40] S. Wiggins, *Introduction to Applied Nonlinear Dynamical Systems and Chaos*, Springer-Verlag, New York, 2nd ed., 2003.

[41] T. Xing, R. Barrio, and A. Shilnikov, *Symbolic quest into homoclinic chaos*, Internat. J. Bifur. Chaos Appl. Sci. Engrg., 24 (2014).

[42] W. Zhang, B. Krauskopf, and V. Kirk, *How to find a codimension-one heteroclinic cycle between two periodic orbits*, Discrete Contin. Dyn. Syst., 32 (2012), pp. 2825–2851.